

# Compact Experimental Negative TriAngUlarUity Reactor (CENTAUR): A design study for a compact, affordable breakeven tokamak

The CENTAUR Collaboration<sup>1,2</sup>, S. W. Freiburger<sup>1\*</sup>, E. Bursch<sup>1</sup>,  
J. Chiriboga<sup>1</sup>, H.J. Farre-Kaga<sup>2</sup>, E. Felske<sup>1</sup>, S. Guizzo<sup>1</sup>, J.  
Labbate<sup>1</sup>, S. Seethalla<sup>1</sup>, F. Sheehan<sup>1</sup>, J. L. Xia<sup>1</sup>, A. Braun<sup>1</sup>, D.A.  
Burgess<sup>1</sup>, N. Chen<sup>2</sup>, J. Halpern<sup>1</sup>, M. Haque<sup>1</sup>, A. Hyder<sup>1</sup>, A.  
Lachmann<sup>1</sup>, R. Lopez<sup>1</sup>, K. Orr<sup>2</sup>, K. Richardson<sup>1</sup>, M. Russo<sup>1</sup>, A.  
Veksler<sup>1</sup>, C. J. Hansen<sup>1</sup>, A. Holm<sup>4</sup>, N. Leuthold<sup>1</sup>, O. Meneghini<sup>3</sup>,  
A. O. Nelson<sup>1</sup>, M. Pharr<sup>1</sup>, T. Slendebroek<sup>3</sup>, I. G. Stewart<sup>1</sup>, F.  
Scotti<sup>4</sup>, M. Tobin<sup>1</sup>, H. Wilson<sup>1</sup>, C.F.B. Zimmermann<sup>1</sup>, and C.  
Paz-Soldan<sup>1</sup>

<sup>1</sup>Columbia University, New York, NY

<sup>2</sup>Princeton University, Princeton, NJ

<sup>3</sup>General Atomics, San Diego, CA

<sup>4</sup>Lawrence Livermore National Laboratory, Livermore, CA

April 2026

## Abstract

This work presents the compact experimental negative triangularity reactor (CENTAUR), a low overnight cost, high-field tokamak, breakeven reactor design, achieving a predicted total fusion power of 40 MW and scientific energy gain of 1.3. Ballooning stability calculations confirm that the device's pedestal is within the first stability regime, which is consistent with the expected ELM-free operation associated with negative triangularity (NT) plasmas. The geometry of the NT divertor allows for high fraction of radiated power (13.5%) between the separatrix and plasma facing components. Heat transport modeling based on simulations of the edge region show heat loads into plasma facing components well below material limits. The magnet system employs rare-earth barium copper oxide (REBCO) high-temperature superconductors in 18 toroidal field coils, an hourglass-shaped central solenoid, and six poloidal field coils to support high-field ( $B_0 = 10.9$  T) plasma confinement, shaping, and current drive. Neutronics analysis shows that a 12 cm  $B_4C$  shield keeps superconducting magnet heating below the 33 K quench limit during 10 s,

40 MW DT pulses. With this shielding, the modeled fluence indicates HTS components can survive more than ten times the 3000-pulse design lifetime. Iteration of economic analysis in tandem with the technical design process allows CENTAUR to achieve its overnight cost goal of \$2B determined using a custom costing model that predicts a total overnight cost of  $1.6\text{B}\pm 0.2\text{B}$ .

## 1 Introduction and Overview

Most experimental tokamaks operate with a positive triangularity equilibrium geometry and achieve maximum performance in High-confinement mode (H-mode). However, H-mode plasmas require high power through the edge region and are prone to periodic, uncontrolled exhaust of heat and impurities in the form of Edge Localized Modes (ELMs) [1, 2, 3]. These events can cause damage to plasma facing components and reduce the operational lifetime of any such device. Negative triangularity (NT) plasmas operate in an ELM-free regime while providing the requisite plasma performance for reactor designs. Further, high-field operation in positive triangularity exposes plasma facing components to extremely high load, creating complex engineering problems for power handling [4]. NT offers the dual advantages of increased radiation, which may be beneficial for detached operation, and increased flexibility in poloidal field (PF) coil placement [5]. The increased capacity to radiate power between the separatrix and the divertor plate protects plasma facing materials from high heat loads. Further, the negative triangularity geometry allows for a broader strike point in the divertor. Device longevity is essential to the economic viability of a future power plant, so the exploration of NT tokamak designs is a valuable area of fusion technology development [6, 7].

This design study explores the potential for an NT tokamak to attain physics gain ( $Q>1$ ) at a sub-\$2B operational cost. This device would serve as a stepping stone towards a larger fusion power plant, such as the proposed Modular Adjustable Negative Triangularity ARC-class (MANTA) device, bringing fusion closer to grid deployment [8]. The study expands on a tradition of fusion design classes, which produced the first ARC design [9] and the design study for the MANTA device. Unlike in positive triangularity devices that achieve maximal operating performance in high-confinement regimes (H-mode), negative triangularity (NT) plasmas can achieve high performance while remaining in a naturally ELM-free state [10].

This paper presents a self-consistent design study of a compact, high-field, breakeven negative triangularity tokamak. The analysis is presented from the plasma core outwards. Section 2 describes the initial scoping of the core scenario and analysis with a more complete integrated core modeling workflow. Section 3 presents core-edge integration and analysis of heat transport between the separatrix and the divertor plates as well as heat transfer modeling for a simplified divertor plate and support structure. Section 4 presents a novel configuration of toroidal field coils to minimize system stresses in an NT geometry and an

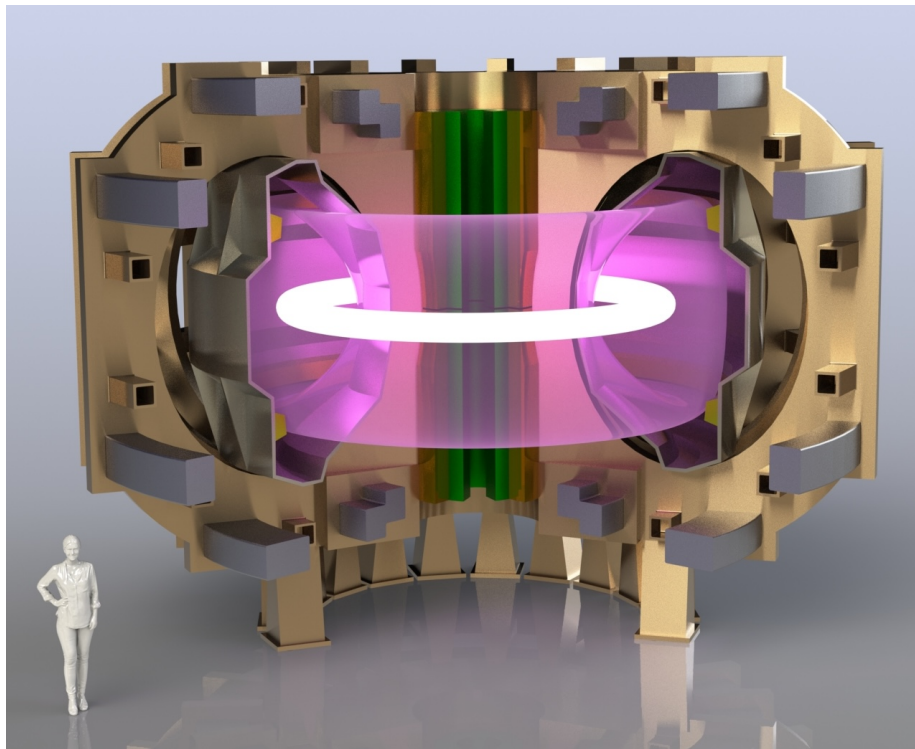


Figure 1: Full CAD render of the CENTAUR design. The volume in pink is representative of the plasma. The metal rendered in gold is the TF casing structure. The gray metal volumes are PF coils, and the green section at the center is the central solenoid.

“hourglass” center stack design to provide the requisite flux swing for startup. This section further presents optimized poloidal field coil placement as well as modeling of stresses from vertical displacement events. Analysis of the impact of neutron damage on system lifetime and neutron heating on magnet performance are discussed in section 5. Finally, section 6 provides costing analysis based on the that in [8], concluding that this device is well within the design target overnight cost of \$2B.

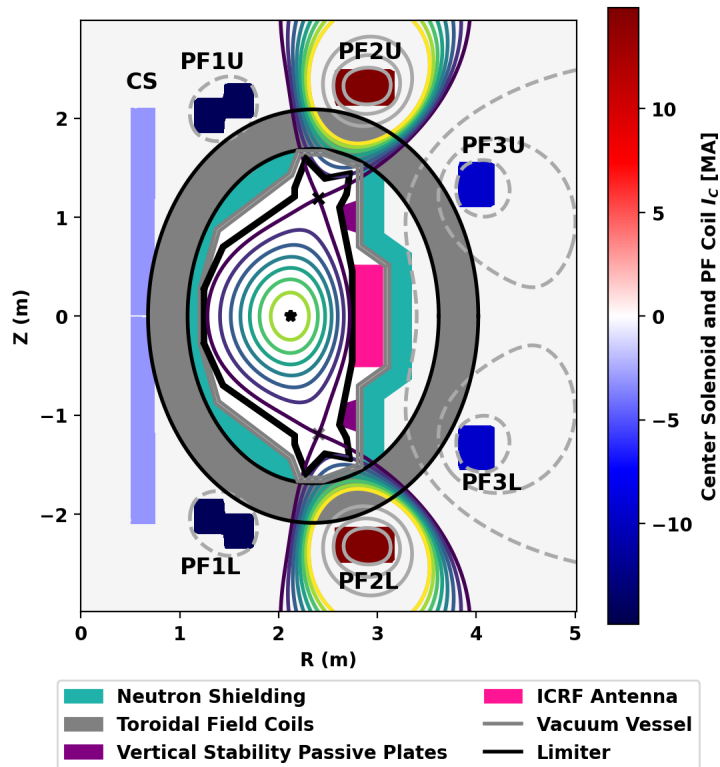


Figure 2: Poloidal cross section showing the primary components and the equilibrium solution produced with TokaMaker [12]

## 2 Core Plasma Scenario

Negative triangularity has significant operational advantages that make it an attractive candidate for the operating scenario in a fusion pilot plant. Notably, NT has demonstrated energy confinement times ( $\tau_E$ ) and normalized beta ( $\beta_N$ ) comparable to H-mode operation while remaining robustly ELM-free [13, 14]. These properties motivate the development of breakeven class NT devices as a step toward a fusion power plant. However, building a  $Q > 1$  experimental

Table 1: CENTAUR Key Design Parameters

Parameter	Symbol	Value
Fusion Power	$P_{\text{fus}}$	40 MW
ICH coupled power	$P_{\text{ICH}}$	30 MW
Scrape-off layer power	$P_{\text{SOL}}$	9.3 MW
Radiated power (core   SOL)	$P_{\text{rad}}$	23 MW   5.4 MW
Radiated power fraction (core   SOL)	$f_{\text{rad}}$	0.62   0.135
Plasma gain	$Q$	1.3
Major radius	$R_0$	2 m
Minor radius	$a$	0.72 m
Elongation	$\kappa_{\text{edge}}$	1.65
Triangularity	$\delta$	-0.55
Plasma volume	$V_p$	29.7 m <sup>3</sup>
Plasma surface area	$A_p$	2.34 m <sup>2</sup>
On-Axis Toroidal magnetic field	$B_0$	10.9 T
Plasma current	$I_p$	9.6 MA
Bootstrap fraction	$f_{\text{BS}}$	0.103
Avg. ion temperature	$\langle T_i \rangle$	5.15 keV
Avg. electron temperature	$\langle T_e \rangle$	4.15 keV
Avg. density	$\langle n \rangle$	$3.21 \cdot 10^{20} \text{ m}^{-3}$
On-axis ion temperature	$T_{i,0}$	14.8 keV
On-axis e <sup>-</sup> temperature	$T_{e,0}$	9.26 keV
On-axis e <sup>-</sup> density	$n_0$	$4.33 \cdot 10^{20} \text{ m}^{-3}$
Average Greenwald fraction	$f_{\text{GW}}$	0.61
$f_{\text{GW}}$ at separatrix	$f_{\text{GW, sep}}$	0.13
Pulse length	$\tau_{\text{pulse}}$	10 s
Normalized beta	$\beta_N$	1.5
Average effective charge ( $\rho = [0, 0.96]$ )	$Z_{\text{eff}}$	1.43
Safety factor at $\Psi_N = 0.95$	$q_{95}$	2.58
Safety factor at $\Psi_N = 0$	$q_0$	1.04
Energy confinement time	$\tau_E$	0.41 s
H <sub>98,y2</sub> confinement factor	$H_{98,y2}$	0.54
H <sub>NT, 24</sub> confinement factor [11]	$H_{NT}$	0.87
Loop voltage	$V_{\text{loop}}$	0.77 V

device requires the identification and modeling of a viable core operating point. This work identifies one possible core operating scenario, providing a concrete starting point for further evaluation of NT as a path toward fusion energy.

## 2.1 0-D Scoping of the Core Operating Regime

The open source code CFSpopcon [15] solves the global power-balance equation [16], generating a 0-D POPCON (Plasma OPERational CONtours) analysis for broad scoping of the initial core operating scenario. Inputs for the POPCON include CENTAUR’s argon impurity concentration, the H98y2 confinement factor, major radius, plasma current, and toroidal magnetic field.

Using the final operating point’s H98y2 confinement factor, the resulting POPCON for CENTAUR in Figure 3 maps fusion power, plasma gain, auxiliary power, and radiative power across electron temperature-density space. The final operating point is depicted as a black star. Notably, the parameter space permits higher fusion power at increased temperature or higher plasma gain at lower densities, giving flexibility for future optimization as NT performance scalings are expanded and validated.

## 2.2 Plasma Core Workflow

Building on the initial operating point scoped by the 0-D POPCONs, the core integrated workflow employs higher-fidelity codes to verify and refine this solution into a realistic, self-consistent core scenario, as depicted in Figure 5. This workflow uses the following code bases: ASTRA [17], a 1.5D modular plasma transport code; TGLF, a quasi-linear turbulence transport code [18]; Toka-Maker, an open source Grad-Shafranov equilibrium solver [19]; UEDGE, a 2D fluid edge transport code [20]; and BALOO, a ballooning stability code [21].

This medium fidelity core modeling workflow begins with a characteristic DIII-D NT electron density profile from experimental data [22], scaled to the the initial operating point determined through POPCON analysis. This initial profile and a Gaussian approximation of an ion cyclotron resonant heating (ICRH) profile then act as inputs to ASTRA. Using the TGLF submodule to model radial transport, the profiles time-evolve to steady state. The convergence criterion is that the change in on-axis electron and ion temperature between successive iterations to be less than 0.01 keV. Profiles from ASTRA are truncated at  $\rho = 0.92$ , where the density and temperature are imposed as interface boundary conditions for UEDGE. UEDGE then solves the scrape-off layer and divertor plasma from the separatrix outward to the wall.

Due to uncertainty and lack of fully predictive NT edge models [23], a cubic spline connects the ASTRA edge at  $\rho = 0.92$  to the separatrix values from UEDGE. Here, the profile shape is modeled after the profile form realized in a large database of high-power NT discharges on DIII-D [23]. BALOO evaluates the stability of this profile to verify that the profile is infinite-n ballooning stable. As shown in Figure 6, the normalized pressure gradient for CENTAUR is well

below the 1st stability limit for infinite n-ballooning modes, as expected for NT ELM-free regimes.

Future work could expand on this study in several important directions, including more realistic heating profiles, higher-fidelity turbulence modeling, and input from broader NT experimental validation. Self-consistent ICRH simulations (instead of the prescribed Gaussian heating profiles) would allow for higher-fidelity treatment of heating deposition. In addition, coupling the present framework with gyrokinetic simulations could provide more accurate treatment of turbulence and transport, particularly in the region near the last closed flux surface (LCFS), allowing for a more accurate characterization of profiles in the plasma edge. Beyond heating and turbulence, introducing density evolution into the simulations through the inclusion of a fueling source, would enable a more complete description of coupled particle and energy transport. A current scan could also provide insight on how plasma performance and stability vary with both the magnitude and profile of the plasma current. Finally, further NT experiments across a wider range of device geometries and magnetic field configurations would be valuable for validating the robustness of NT core predictions and assessing their generality across different tokamak regimes.

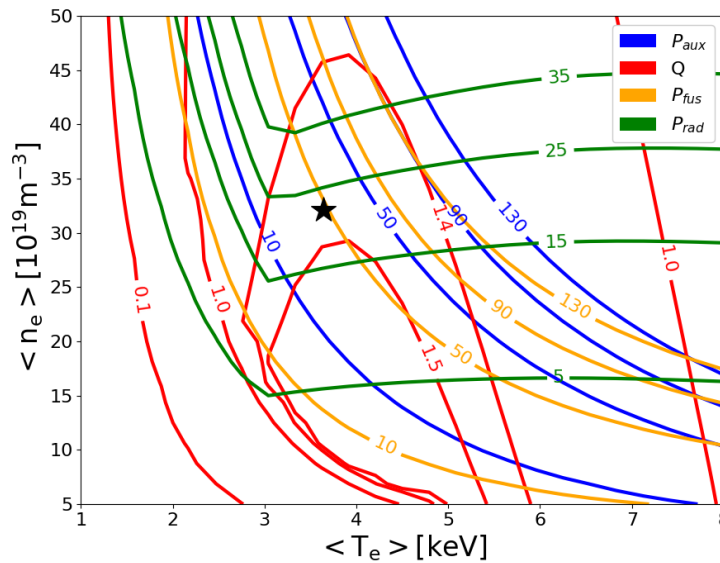


Figure 3: POPCON visualization of parameter space surrounding CENTAUR’s operating point. The intended operating point is marked with a black star.

### 2.3 Transport simulation with TGLF in ASTRA

The ASTRA modeling [25, 26] framework, coupled to the TGLF turbulence code [27], simulates transport in CENTAUR. ASTRA solves the time-dependent 1D

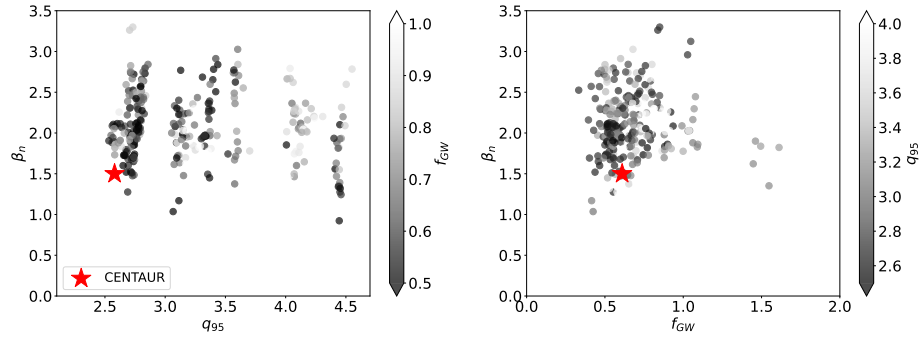


Figure 4: Operating point indicated by stars at  $\beta_N = 1.5$ ,  $f_{GW} = 0.61$ , and  $q_{95} = 2.58$ . Operational space data from supplementary data supplied with the work by Paz-Soldan et. al. [24]. Stars indicate where the CENTAUR operating plot falls within operating space of strongly shaped, negative triangularity plasmas on DIII-D.

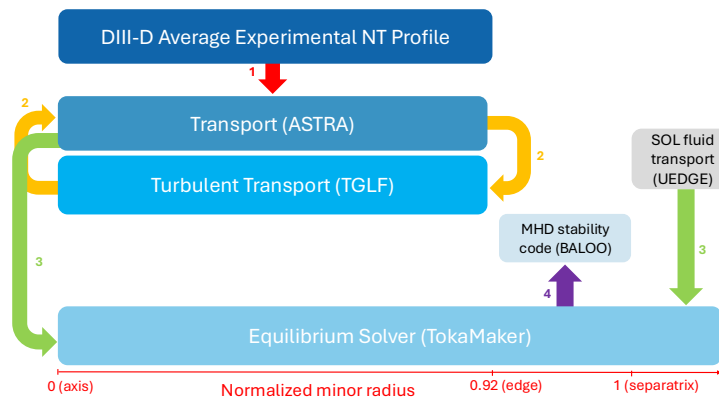


Figure 5: Integrated modeling flowchart showing the codes used over various  $\rho$  regions and the iterative steps between them.

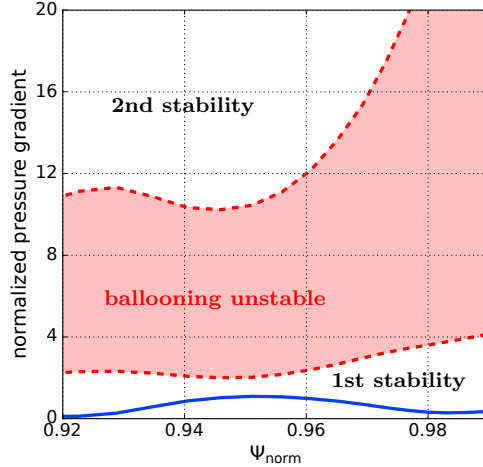


Figure 6: The normalized pressure gradient (blue curve) occupies the 1st stability region below the ballooning unstable curve (red) calculated by the BALOO code.

transport equations with turbulent fluxes provided by TGLF. All TGLF runs use the SAT2 saturation rule, which has been shown to be sufficient for NT plasmas [28, 29]. The simulation includes electrons, a 50/50 mix of deuterium/tritium (D-T), and argon with an average impurity density of  $n_{\text{Ar}} = 8.1 \cdot 10^{17} \text{m}^{-3}$ . Preliminary scans of the impurity density find that CENTAUR’s performance remains relatively robust, with increasing the average impurity density by 11% only resulting in a decrease of fusion gain by 8%. Further modeling of impurity transport is out-of-scope for the present analysis. This argon impurity is implemented in ASTRA through a prescribed average core  $Z_{\text{eff}}$  of 1.4, which monotonically increases from 1.0 at  $\rho = 1.0$  to 1.6 at  $\rho = 0.92$ . Bremsstrahlung and line radiation are also self-consistently included. The temperature profile is evolved until to a steady state, with the density profiles held fixed to an edge electron density of  $n_{e,\text{ped}} = 2.55 \cdot 10^{20} \text{m}^{-3}$  and edge electron temperature of  $T_{e,\text{ped}} = 1.8 \text{keV}$  at  $\rho = 0.92$ . These boundary conditions are selected to reflect a pedestal sufficient to achieve  $Q > 1$ , as the NT edge pressure pedestal is closely correlated with overall plasma performance [30]. The ASTRA-TGLF simulation is limited to  $\rho = 0.92$  as TGLF does not capture pedestal physics and cannot properly model the edge region in NT; similar approaches have been adopted in previous ASTRA-TGLF studies of NT plasmas with simulation boundaries extended to  $\rho \approx 0.94 - 0.95$  [29, 31].

Figure 7 displays the resulting density, temperature, and power density profiles from the converged ASTRA-TGLF simulation. Figure 7(a) shows the ion (blue curve) and electron density profiles (red curve). The electron density profile and  $Z_{\text{eff}}$  are held fixed, while the ion and impurity densities are calcu-

lated to enforce quasi-neutrality; the slight deviation between the electron and ion densities is due to argon impurity density. The ion density represents the combined deuterium and tritium density. Figure 7(b) shows the temperature profile where on-axis  $T_{e,0} = 9.26$  keV and  $T_{i,0} = 14.8$  keV are predicted. The ion temperature profile has stronger peaking in the core relative to the electron temperature due to the prescribed axis-centered ICRH heating profile, shown in 7(c) (black dashed line). Figure 7(c) depicts the power density profiles, including the ion and electron heat fluxes, auxiliary heating, and fusion power. The auxiliary power (black dashed line) is on the same order of the fusion output power (green line), which is expected for a  $Q \approx 1$ . The ICRH heating deposition mainly contributes to the ions, which explains why the total ion flux (red line) is larger than the electrons (blue line). The peak fusion power density at the core is  $P_{\text{fus},0} = 35$  MW/m<sup>3</sup>.

A more consistent and radially resolved analysis of the core impurity transport is left for future work and would require using neoclassical and impurity transport codes as discussed by Fajardo et al. [32]. Nonetheless, the final operating point, as seen in Figure 4, falls within the NT operating space defined by the DIII-D database of stationary, strongly-shaped, diverted NT plasmas; confirming that the simulated operating point is consistent with experimentally achieved NT conditions.

## 2.4 Vertical Stability

Vertical stability is assessed through TokaMaker time-dependent stability simulations, further explained in [33], with the simulation results and vertical stabilization hardware shown in Figure 8. Figure 8b) shows that with the addition of targeted tungsten passive plates and assuming a control coil maximum voltage of 15 V, an estimated 14.5% perturbation of the minor radius, or 10.4 cm, can be stabilized. This is a larger value than most existing tokamaks [34], suggesting CENTAUR is sufficiently vertically stable. The 15 V limit for AC superconducting coils is estimated from [35].

A metric for characterizing the controllability of VDEs is the feedback capability parameter, or the product between VDE growth rate  $\gamma$  and wall diffusion time  $\tau_W$ . CENTAUR has a VDE growth rate  $\gamma \approx 12$  s<sup>-1</sup> and a wall diffusion time  $\tau_W \approx 30$  ms, leading to  $\gamma\tau_W \approx 0.36$ , significantly more stable than a typical target controllable feedback capability parameter of  $\gamma\tau_W \lesssim 1.5$  [33]. Overall, the simulations suggest CENTAUR is sufficiently vertically stable despite the presence of the vacuum vessel and shielding between the control coils and the plasma. As a result, significant margin likely exists to further increase elongation for possible performance improvements.

## 3 Power Handling and Divertor Design

Any break-even magnetic confinement device must contend with managing substantial particle and heat loads from the plasma [36, 37, 38, 39, 40, 41, 42,

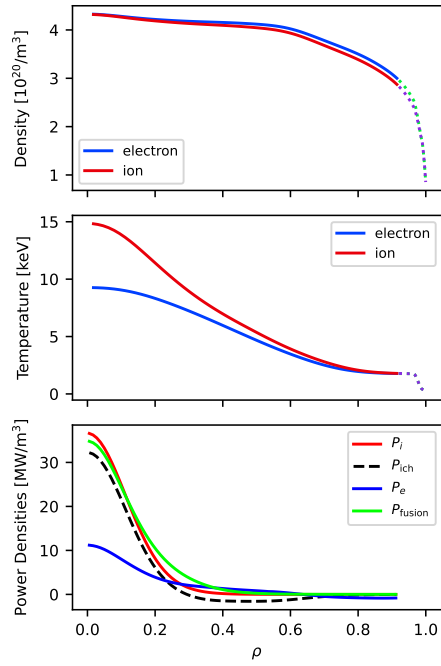


Figure 7: Selected ASTRA profiles as a function of  $\rho$ . The dotted segments for  $\rho > 0.92$  indicate values beyond the ASTRA computational boundary: (a) electron and ion density profiles, (b) electron and ion temperature profiles, (c) power density profiles, including auxiliary heating, ion and electron heat fluxes, and fusion power

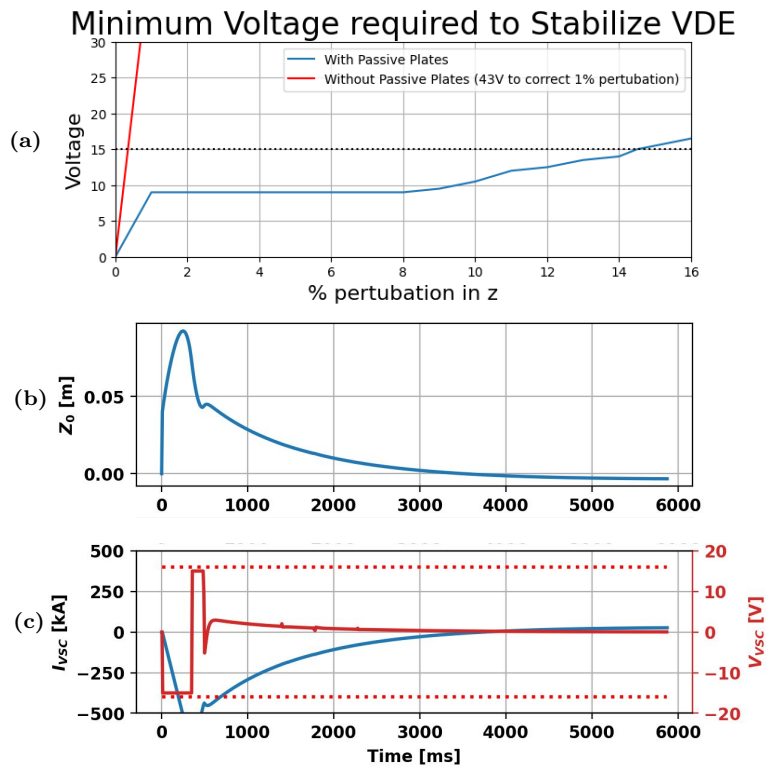


Figure 8: (a) Vertical control coil voltage needed to stabilize plasma for a given initial perturbation scale. (b) Vertical position of the plasma over time in the case of a 14.5% perturbation. (c) Control coil voltage and current over time in the case of a 14.5% perturbation.

Table 2: UEDGE Simulation parameters and  $\lambda_q$  comparison. Eich H-mode[45] scaling yields  $\lambda_{q,\text{OMP}} = 0.37$  mm, Scarabosio L-mode[46] scaling yields  $\lambda_{q,\text{OMP}} = 3.28$  mm.

Parameter	Simulation value
$P_{\rho=0.96}$	17.84 MW
$n_{i,\rho=0.96}$	$2.15 \times 10^{20} \text{ m}^{-3}$
$\lambda_{q,\text{OMP}}$	1.56 mm

43]. Most tokamak designs concentrate the bulk of these loads onto a specifically designed part of the device, known as the divertor. Typically, the divertor uses wall materials that are designed to withstand the heat loads and radiative power exhaust (such as impurity radiation) to reduce the target loads. Negative triangularity devices are envisioned to operate in conditions more comparable to L-mode than H-mode. As a pedestal is not required,  $P_{\text{SOL}}$  does not need to be more than the L-to-H-mode transition power ( $P_{\text{LH}}$ ), so higher impurity fractions can be used [3]. With increased impurity radiation, advanced divertor techniques like strike line sweeping may no longer be needed to keep the maximum perpendicular heat flux below  $10 \text{ MW/m}^2$  on the tungsten divertor plates [44].

### 3.1 Scrape-off Layer Simulation and Core-Edge Integration

The UEDGE 2-D multi-fluid, edge-plasma code models the scrape off layer and self-consistently predicts the particle and heat loads on the divertor plates [20, 47]. UEDGE solves the Braginskii fluid equations, including ionization, recombination, and impurity radiation. The code also includes anomalous cross-field diffusion to approximate turbulent cross-field transport. Cross-field particle and heat transport coefficients are manually/iteratively matched to follow empirical scaling laws for the heat flux width [45, 46]. Due to a lack of experimental characterization of diffusivity in the NT edge, diffusivity coefficient profiles in the SOL are set to be constant along magnetic field lines with stepwise changes perpendicular to the magnetic field, see Figure 10. The amplitude of this profile over the mesh is decreased until a moderately H-mode biased  $\lambda_q$  for the no impurity seeding base case is achieved, and is held constant in subsequent case iterations.

The UEDGE mesh (Figure 9) is generated with input magnetic equilibrium from TokaMaker [48]. Each divertor plate is approximated as a line segment created at the mesh-vacuum interface in the divertor region. To save computational cost, only the lower half of the device has been simulated, and the input power is halved accordingly. Note that  $\nabla B$  drift biases the power split away from 50/50, but in operation, the plasma can be moved vertically to recover a 50/50 split.

The inner mesh boundary is positioned at  $\rho = \sqrt{\psi_N} = 0.96$ . The primary

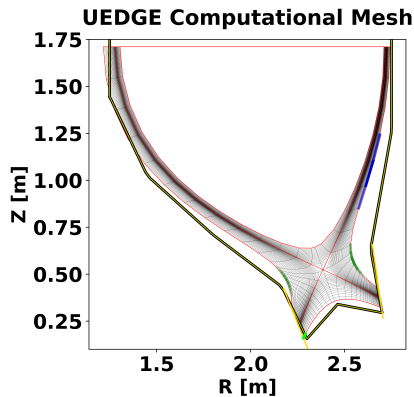


Figure 9: The UEDGE Computational mesh, configured to be from normalized poloidal flux  $\psi_N \approx 0.93$  to  $\psi_N \approx 1.078$  on the outboard side. Limiter (black & yellow) is shown along with the computational divertor plates (yellow). The separatrix is in red. Deuterium gas fueling is in dark blue. Both neon gas puffs (next to the X-point) are shown in dark green. Species pumping (light green) is in the low field side (inboard side) private flux region.

UEDGE inputs (power and density) at this core-edge boundary are produced by ASTRA and detailed in Table 1. The NT-like  $T_e$  pedestal is matched with the resulting UEDGE outer midplane electron temperature,  $T_{e,omp}$  value at  $\rho = 0.99$ . The BALOO infinite-n ballooning stability code also validates the pedestal. An exponential fit to the UEDGE outer midplane electron heat profile is used to characterize  $\lambda_q$  (and is shown in Table 1 and Figure 11). NT  $\lambda_q$  has been observed to lie between the upper bound of L-mode scaling and the lower bound of H-mode scaling, skewed toward H-mode. In NT scenarios on DIII-D,  $\lambda_q$  has been experimentally measured between 1.5 mm and 3.5 mm. These values fall within the range of H-mode and L-mode scalings, with a bias toward H-mode width. [1]. Given the device parameters, the Eich et al. [45] H-mode scaling yields  $\lambda_q = 0.37$  mm, while the Scarabosio et al. [46] L-mode scaling yields  $\lambda_q = 3.28$  mm. These two values are used as upper and lower bounds for the  $\lambda_q$  space, respectively.

A linear radial extrapolation boundary condition is used for  $n_i$ ,  $T_i$ , and  $T_e$  on the outer wall. The ion density is fixed to  $n_{i,PFR} = 10^{18} \text{ m}^{-3}$  at the private flux region wall. The private flux region is the region below the X-point and between the strike lines. The ion and electron temperature also use a linear radial extrapolation boundary condition on the private flux region wall.

### 3.1.1 Fixed Fraction Impurity Model

Initial UEDGE simulations employ the fixed-fraction model for neon in the plasma edge. In this model, the impurity density is set to be a fraction of the ion density,  $n_{imp} = n_i/f_{imp} = 0.032$ , and only accounts for neon radiation. The

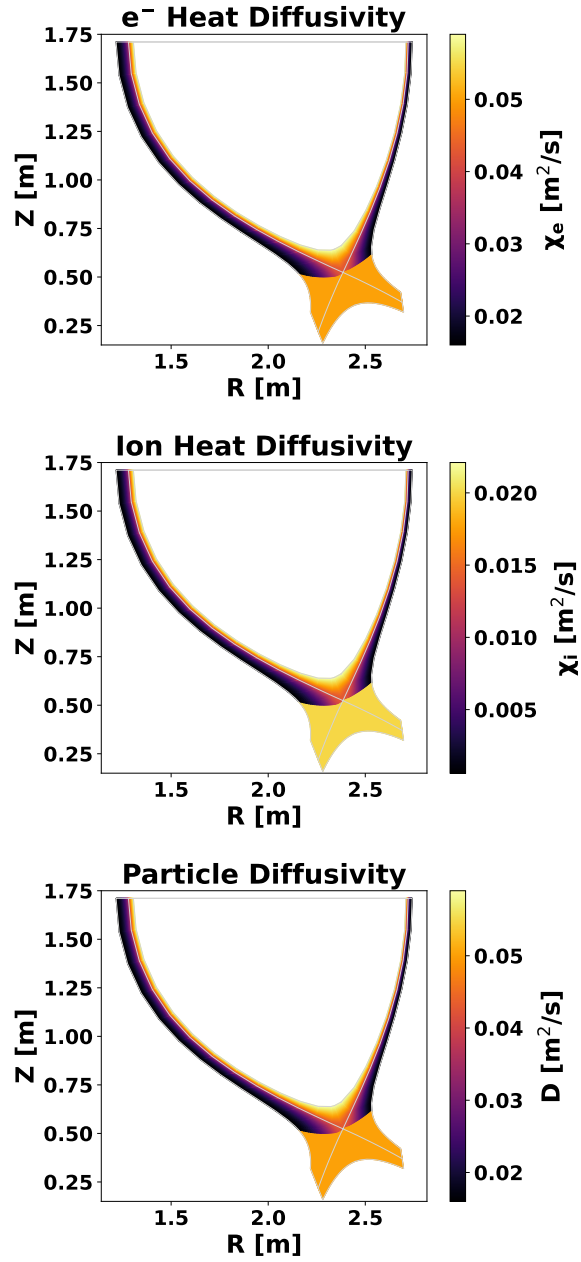


Figure 10: Imposed electron heat, ion heat, and particle cross-field diffusivity coefficient profiles, set cell-by-cell, incrementally decreasing over radial indices.

model does not consider any impact on particle balance and leaves  $Z_{eff}$  unchanged. User-specified  $f_{imp}$  can be spatially varying distributions. Collisional-radiative effective impurity rates are used to assess the enhanced radiation due to impurities. We follow the MANTA design approach by seeding different noble gases in the core and edge to optimize radiative cooling. Neon has been chosen as the impurity species in the edge region for all configurations due to its strong radiation properties and lower atomic number ( $Z$ ) compared to other species, such as Argon. We assume that the impurities do not significantly mix: i.e. core-injected Argon is assumed to remain largely in the core, while the divertor puffed Ne is fully ionized before reaching the core. Under these conditions, the dual-species approach is an acceptable modeling approximation to achieve the desired radiation distribution. Detailed impurity transport modeling to refine these assumptions should be included in future work.

The model is set up to fuel the plasma with deuterium on the high field side lower wall, and user-placed pumps can be used for particle balance. For this design, the pump has been placed at the corner of the private flux region (PFR) and the outer divertor plate, as shown in Figure 9.

### 3.1.2 Force Balance Model

Impurities in UEDGE can also be treated as additional ion and gas species for each charge state and include physics like ionization and recombination between charge states, inter-species friction, and thermal forces. This model, coined force balance (for the parallel velocity equation when impurity inertia and viscosity are ignored [49]), can better model the separation between neon charge states and adds control over where impurities are added to the system as a gas species. Figure 9 shows the two neon gas puffs in green near the X-point.

Similarly to deuterium, another pump is added in the private flux region near the outer divertor plate that only removes neon. The two neon puffs now give control over how much power is radiated in the outer and inner half of the SOL, and this ratio can be modified by changing the ratio of the gas puff amplitude. The deuterium fueling and pumping location was kept the same as the Fixed Fraction model. Scotti et al. [50] investigated the out/in power asymmetry in DIII-D for different magnetic field directions and different triangularities.

The neon charge states have the same core momentum and current boundary condition as deuterium. The outer and PFC wall boundary condition uses a gradient scale length approximation, with the minimum wall density being  $10^7 m^{-3}$ . This boundary condition gives more freedom than the extrapolation boundary condition. The fluid neutral model limits the convective transport to the free-streaming flux using flux limiters. The neutral gas flux limiters are adjusted to attain numerical stability of the convergence

## 3.2 Power Deposition

In the final fixed fraction impurity scenario, an exponential fit to the OMP radial electron heat flux profile in Figure 11 yields  $\lambda_{q,OMP} = 1.56$  mm, within the

bounds of L-mode and H-mode scalings. The smallest plasma-wall separation occurs at the inner midplane (IMP): 2.1 cm.  $\lambda_{q,IMP} = 1.02$  mm, resulting in  $T_{e,IMP\ wall} = 7.48$  eV. This is below both the 10 eV tungsten sputtering limit and the 8 eV retention energy threshold [51, 52].  $T_{e,IMP\ wall}$  is a direct result of the radial temperature falloff length. Consideration of interchange, magnetic curvature, turbulence, and sheath physics in the edge is necessary for a more physics-informed wall temperature.

UEDGE is used to scan inner and outer divertor plate angles to identify the angles that minimize heat flux and neutral backflow into the plasma. The length of the divertor plates is also a factor. Closing the divertor more forces the plates to either intersect plasma near the X-point or intersect the existing vacuum vessel design. The optimal inner and outer plate angles given spatial constraints are  $45^\circ$  and  $58^\circ$ , respectively.

The final inner and outer plate heat fluxes are shown in Figure 12, with the results from the fixed fraction and the force balance model shown on the top and bottom rows, respectively. The peak heat flux of  $7.9$  MW/m<sup>2</sup> is below the steady-state tungsten limit of  $10$  MW/m<sup>2</sup>.  $P_{SOL} = 9.424$  MW and  $f_{rad, UEDGE} = P_{rad, UEDGE}/P_{fus} = 20.6\%$ , for the fixed fraction model. In contrast,  $4.83$  MW of power is radiated by impurities and hydrogen in the force balance model (inside the whole computational domain). Using this value, the injected power and alpha power, the model finds  $f_{rad, UEDGE} = 13.7\%$ . For both models, the ion density is higher in the outer divertor, while the electron temperature is lower. Even in the hotter inner divertor, the peak electron temperature is below the  $\approx 13$  eV sputtering and  $\approx 8$  eV retention energy thresholds [51] [52]. Both plates are also lower than the tungsten deuteride molecule sputtering energy threshold [53]. It's worth noting that the temperature is a Maxwellian, and the closer it gets to the sputtering threshold, the more of the distribution tail will exceed the threshold energy.

One solution to the heat and particle flux challenge is to reduce the energy and momentum of the plasma via radiation and collisions. In this regime, called the radiative plasma detachment regime, a large part of the plasma neutralizes and slows down in a layer above (detached from) the target plate [54, 55]. While there are many signals for plasma detachment, it has been found that the target heat flux profile broadens and decreases in amplitude [56, 57, 58, 59]. Initial detachment studies used the fixed fraction model to quickly scan the global neon fraction. Figure 13 shows this scan of peak perpendicular heat flux and heat flux full width half max (FWHM) over neon fraction. As more neon is seeded, both peak heat fluxes drop. At the same time, the width of the heat flux profiles increases, point to the possibility of divertor detachment. More detailed detachment studies are left for future work and will likely require the force balance model to look at local neon and deuterium density build-up near the plate, as well as recombination.

Figure 14 shows the power radiated by neon in the whole domain using the force balance model. As expected, most of the power is radiated near the X-point and along the strike line. The effective charge  $Z_{eff} \approx 1.66$  along the separatrix, which is close to ASTRA's prescribed  $Z_{eff} = 1.6$ . Further work

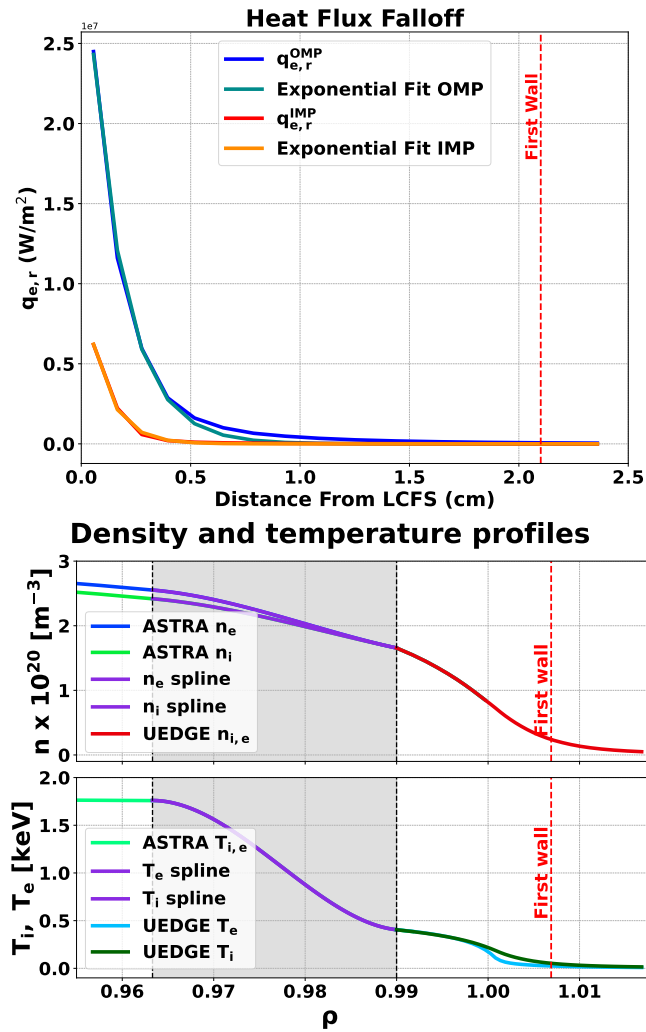


Figure 11: Electron heat radial falloff outside the LCFS at the midplane (left).  $\lambda_q$  was found by applying an exponential fit (also shown) to the electron heat flux profile. Outer midplane wall kinetic profiles (right), including the cubic spline (grey shaded region bounded by dashed lines) that stitches ASTRA and UEDGE.

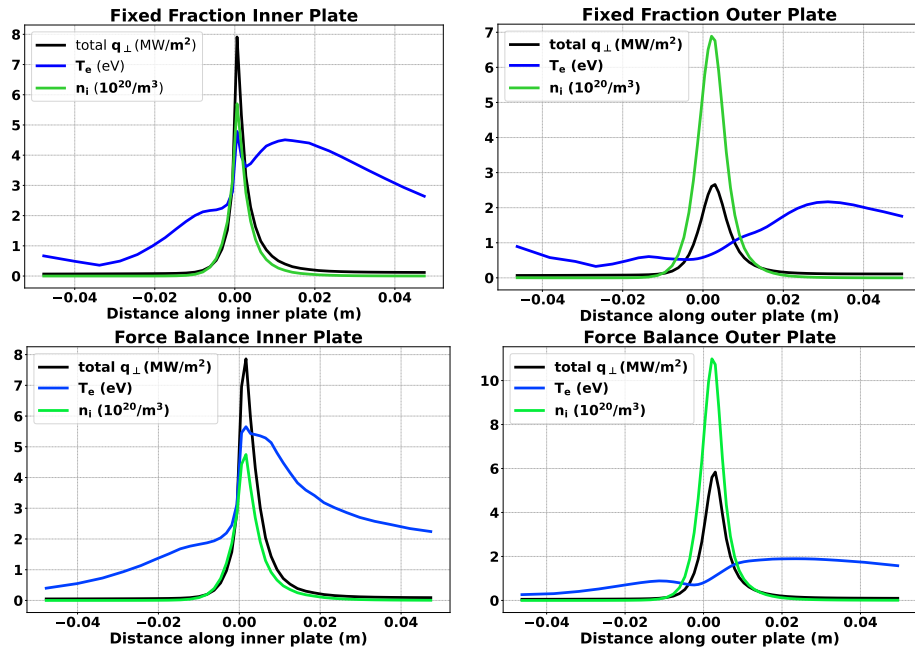


Figure 12: Inner (left column) and outer (right column) divertor plate perpendicular heat flux, electron temperature and main ion density profiles along the respective plate. Top row is profiles from fixed fraction 3.2% Ne seeding. Bottom row is profiles from the force balance model. Note the differences in imposing a power splitting ratio via localized impurity seeding in the force balance case.

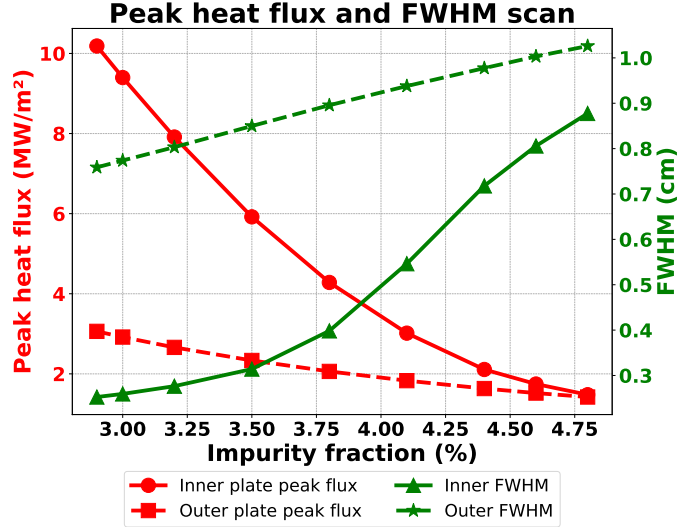


Figure 13: Peak perpendicular heat flux (red) and full-width-half-max (FWHM) of heat flux profile (green) as Ne seeding (in the fixed fraction model) is increased.

should include changing the core boundary condition and neon seeding location to match the separatrix  $Z_{eff}$  between UEDGE and ASTRA. Matching  $Z_{eff}$  would also require more accurate neon upstream transport modeling.

### 3.3 Heat Transfer Modeling

The peak heat flux into the divertor plates is  $<10 \text{ MW/m}^2$ , less than the ITER steady-state limit as expressed in the ITER divertor physics baseline [60], so conditions in the divertor region are expected to be below critical material limits for tungsten plates. A Gaussian flux profile fit to the heat flux profile from UEDGE serves as input to a COMSOL heat transfer model of the divertor plates and substructure. The time dependence of the flux over the shot is represented via a piecewise linear function.

The heat transfer model predicts a maximum temperature on the divertor plate of  $\sim 310 \text{ C}$  over a thirty second pulse. The assumption of simple rectangular block components offers sufficient model accuracy while allowing for flexibility in the final design of the experiment. Figure 15 displays the temperature map of the structure from divertor plate through to an external passive cooling channel at peak operational temperatures. The COMSOL geometry spans from the 1 cm tungsten divertor plate, through a steel mounting plate, a structural foot, the vacuum vessel, and ends at a passive carbon dioxide cooling channel to deliver coolant between shots. The tungsten plasma facing components operate with a maximum temperature below 300 C, well below the recrystallization tempera-

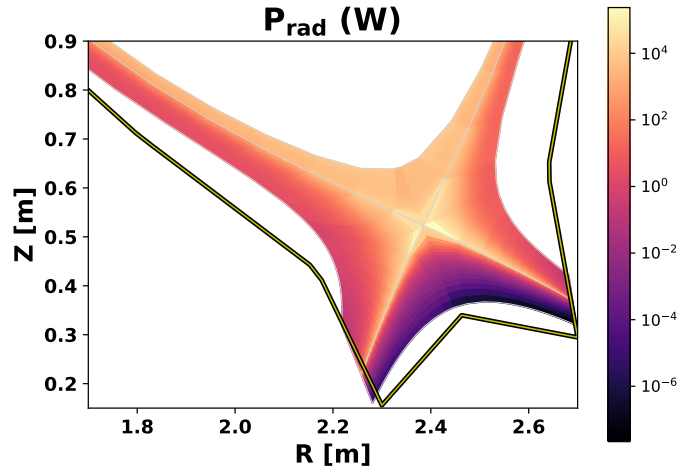


Figure 14: Power radiated in the computational domain calculated by the UEDGE force balance model.

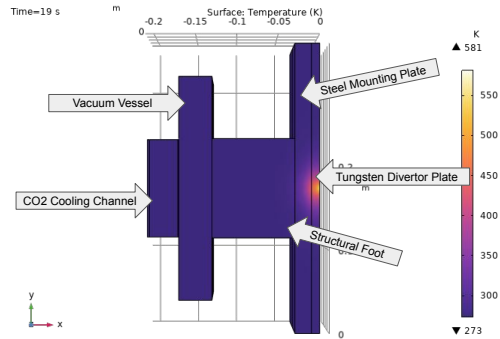


Figure 15: Simplified representation of the region between the divertor plate and the cooling channel outside the vacuum vessel showing the temperature at its maximum value in a time-dependent simulation of heat transfer in a full-performance shot. The tungsten plate remains well below its recrystallization temperature.

ture of 1500 C [61]. This operating state ensures that the device will withstand the conditions of full-performance pulses. The strong divertor performance seen here is a feature of the highly radiative NT divertor region and implies that future iterations of this device could withstand higher performance operating points those explored here.

## 4 Magnets and Device Structure

The CENTAUR magnets are designed to meet the high magnetic field requirements of the plasma core scenario while remaining within practical engineering and cost constraints. All major magnet components employ Rare-Earth Barium Copper Oxide (REBCO) high-temperature superconductors (HTS). REBCO has been utilized in the production of high-current, high-field magnets for fusion applications, demonstrating impressive performance at strong magnetic fields [62, 63]. The final system consists of 18 toroidal field coils, a central solenoid, and a set of six poloidal field coils that together provide plasma confinement, shaping, and Ohmic current drive.

### 4.1 Toroidal field coils

The toroidal field coils achieve an on-axis magnetic field of 10.9 T, with a maximum field of 23 T on the magnets themselves. The peak magnetic field ripple on the plasma boundary is 0.34% at the outboard midplane (OMP). Each high-temperature superconducting winding pack is composed of discretely wound pancakes stacked within a steel case, similar to the design of the SPARC Toroidal Field Model Coil [62]. The dimensions of the CENTAUR toroidal field coils allow for 15 pancakes per winding pack, with 16 turns of superconducting tape stacks per pancake. Each tape stack is composed of 240 REBCO tapes. Each tape has dimensions of 4 mm by 14.4 mm.

To produce a 10.9 T field at the plasma magnetic axis, each toroidal field coil carries 6.06 MA of current, with an operating current of 25.25 kA per HTS tape stack. The resulting HTS current density of 440 A/mm<sup>2</sup> has a 56% margin on the critical current density of 1000 A/mm<sup>2</sup> at 20 K and 25 T perpendicular magnetic field, determined from experimental data on commercially available superOx tapes [64]. Using the approximate leading order dependence of the critical current density on temperature from [65] and fitting the scaling law to the reported performance of superOX tapes at 4.2 K and 20 K from [64], the critical temperature at a 25 T field is estimated to be approximately 33 K. Over a 10 s plasma discharge, neutron heating is expected to raise the HTS temperature to a maximum of 27 K without active cooling, as discussed further in section 5. The HTS is therefore likely to remain below its critical current throughout the discharge. Future work will involve modeling the active cooling of the toroidal field coil magnets to obtain more robust predictions for the HTS operating margin. A summary of the major toroidal field coil parameters can be found in Table 3

Table 3: Toroidal field coil parameters.

Parameter	Value
Number of TFs	18
Winding pack radial thickness	0.4 m
Winding pack azimuthal thickness	0.24 m
Pancakes per TF	15
Pancakes azimuthal thickness	12 mm
Turns per pancake	16
REBCO tapes per turn	240
Width of each REBCO stack	14.4 mm
Height of each REBCO stack	4.0 mm
Winding pack current	6.06 MA
Current per turn	25.25 kA
Operating current density	440 A/mm <sup>2</sup>
Peak magnetic field on winding pack	23 T

A traditional “Princeton Dee” [66] toroidal field coil shape is not considered for CENTAUR due to the large magnet volumes it would require to accommodate the negative triangularity shape. Instead, both oval and conformal “negative triangularity” magnet shapes are analyzed for stress. COMSOL simulations suggest that the conformal magnet experiences higher peak stresses in the magnet lobes than the oval magnet, and an oval magnet is thus chosen for the final toroidal field coil design.

## 4.2 Central solenoid

In contrast to toroidal field coils, the central solenoid leverages PIT VIPER technology, where REBCO tape stacks are arranged in petals to form cables for use in pulsed HTS magnets. PIT VIPER cables have been tested under several loading conditions and are predicted to sustain 50 kA per cable at 20 K and 25 T magnetic field [35].

The design of the central solenoid is primarily constrained by the flux swing requirements of the plasma core scenario. Using the analytic approximations from [67], an estimated 40.9 Wb of flux is required for startup in CENTAUR. An additional 7.7 Wb is needed to sustain the 10 s target flattop. This value is calculated by estimating the loop voltage from core plasma parameters using Spitzer resistivity, including corrections for  $Z_{\text{eff}}$  and neoclassical effects. Future work will involve higher fidelity start-up simulations in order to refine the plasma flux swing requirements. The overall requirement of 48.6 Wb is challenging given the constrained inboard radial build. Furthermore, to produce a negative triangularity shape, the flux swing produced by the poloidal field coils detracts from the flux swing produced by the central solenoid, in contrast to positive triangularity where the effect is additive [68]. To produce additional flux, the central solenoid is extended to include additional windings above and below the

toroidal field coils at larger major radius, which is enabled by the elliptical TF shape.

The outer radius of the solenoid at the midplane is limited to  $R = 0.68$  m by the position of the toroidal field coils. To determine the optimal dimensions of the extended central solenoid, we perform a 2D scan of the solenoid inner radius and the outer radius of the solenoid extension and quantify the available flux swing, taking into account the field produced by the poloidal field coils. The results in figure 16a map out the flux swing produced by several geometries, and indicate which designs result in peak fields larger than the PIT Viper testing conditions [35]. The chosen design point, shown in figure 16b has an inner radius of  $R = 0.51$  m, an extended outer radius of  $R = 0.75$  m, and produces a total flux swing of 52 Wb. When accounting for the flux detracted by the ramp-up of the poloidal field coils, the flux available for the plasma is just sufficient to meet the plasma startup and flattop requirement. While modest, the extension to the central solenoid is necessary for the CENTAUR design, with 30% of the flux being produced by the windings away from the midplane. At full solenoid current of 89.8 MA, The maximum field on the solenoid is 25.8 T, which is marginally higher than the maximum field tested on PIT Viper cables. Further optimization of the central solenoid dimensions, including scans of the central solenoid height, may open opportunities to reduce the peak field while maintaining the available flux swing.

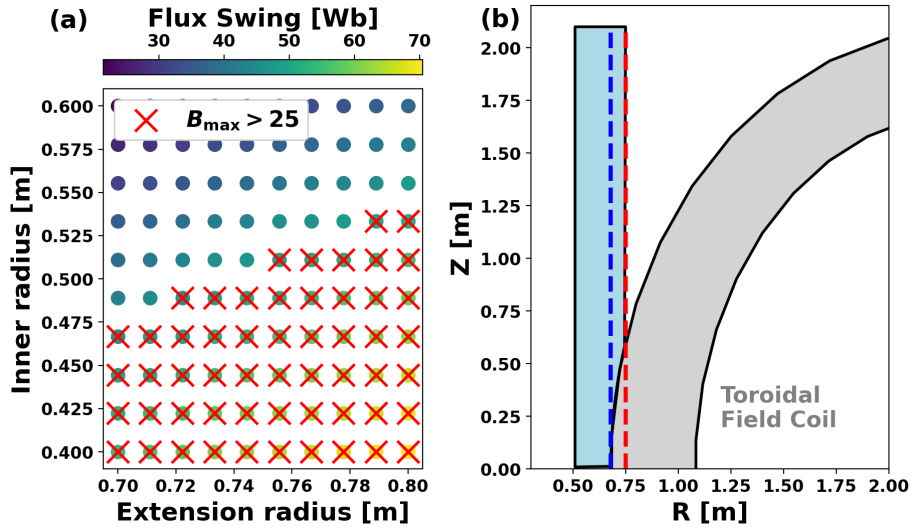


Figure 16: (a) Solenoid flux swing as a function of solenoid inner radius and outer radius of the solenoid extension and (b) schematic of the CENTAUR central solenoid, which is extended with additional turns around the toroidal field coils between  $R = 0.68$  m and  $R = 0.75$  m in order to meet the flux requirement.

### 4.3 Poloidal Field Coils

The poloidal field (PF) coils are also designed as PIT VIPER HTS multi-turn coils. The PF coil set includes six coils with up-down symmetry. In order to use HTS PF coils, they must be positioned outside of the TF coils to allow machine assembly without requiring jointed HTS magnets, which are not a mature technology. This relieves any PF coil position restriction based on neutron heating because the center stack and TF coils are both shown to be able to sustain the higher neutron flux they will experience closer to the plasma.

The PF coils are modeled using TokaMaker as regions of uniform current density in the 2D cross section, shown in Figure 17. The positions of the coils are optimized via a brute-force scan of possible coil positions while maintaining up-down symmetry. The goal of this scan is to minimize the largest PF coil current while producing the core scenario equilibrium targets. Figure 17 shows an example of sampled PF coil locations. Every combination of PF coil positions (where the up-down pairs were moved together to maintain symmetry) is used to produce an equilibrium. The solution with the smallest maximum current in any PF coil where the target equilibrium parameters are achieved is chosen.

Using the same 50 kA per turn limit as the center solenoid and VIPER cable dimensions of 2.3 cm by 2.3 cm, a current density limit is calculated to be 95 MA/m<sup>2</sup> [35]. The coil cross-sections are configured to minimize currents by bringing the current carrying regions closest to the plasma, without exceeding the current density limit or requiring angled cross sections which would produce conical magnet casings. The TokaMaker model is run with three fixed CS coil currents representing the extrema and the average states over the flux swing: +89.8, 0, and -89.8 MA. PF coil design details, currents, and current densities at the three CS states are shown in table 4. All coils under all conditions modeled thus have significant margin before the current density limit discussed above. Future work will include systematic optimization of the position and design of the PF coils over an entire simulated pulse.

Table 4: Poloidal field coil cross-sectional areas, currents, and current densities at three center stack coil currents. The PF coils are up-down symmetric, as is the plasma, so these data are presented for Upper (U) and Lower (L) pairs. Figure 17 shows the locations of the coil.

$I_{CS}$ [MA]	Quantity	PF1U/L	PF2U/L	PF3U/L
	Area [ $m^2$ ]	0.195	0.216	0.162
-89.8	$I_{PF}$ [MA]	-16.4	13.9	-10.1
0	$I_{PF}$ [MA]	-14.2	14.9	-9.6
+89.8	$I_{PF}$ [MA]	-12.0	15.9	-9.1

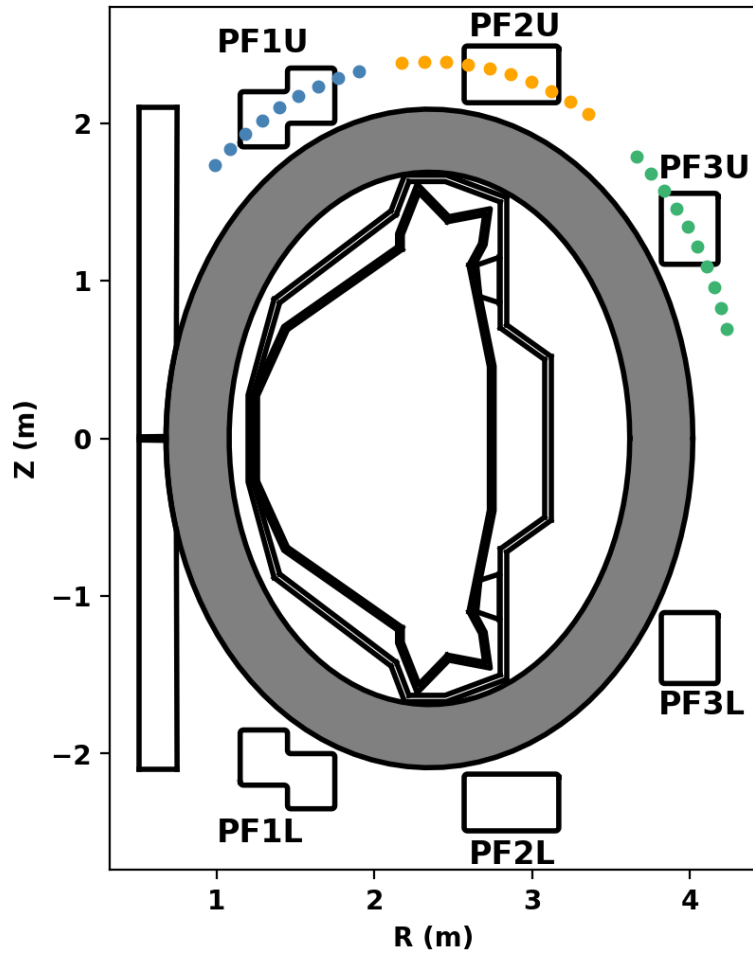


Figure 17: Cross section of CENTAUR with PF coils locations where blue, orange, and green circles show a set of locations sampled for PF1U/L, PF2U/L, and PF3U/L, respectively. Up-down symmetry was maintained, meaning the PF coil pairs were moved together. Each combination of coil positions was used to produce an equilibrium solution with TokaMaker, and the locations producing the lowest maximum coil current while producing the required core plasma parameters was selected.

#### 4.4 Structure and mechanical stresses

Each toroidal field coil is surrounded by a case of Nitronic 40, a favorable structural material due to its high yield stress. The case is approximately 2.7 cm thick on all sides. Additional Nitronic 40 structure is included around the poloidal field coils and in between the toroidal field coils and central solenoid, as shown in Figure 18. The toroidal field coils are bucked against the solenoid to withstand the radially inward centering force. A plug made of non-magnetic resin is included in the central solenoid to combat the large radially inward force on the solenoid when it has no current. Additional Nitronic 40 brackets are included between toroidal field coils to withstand the overturning force.

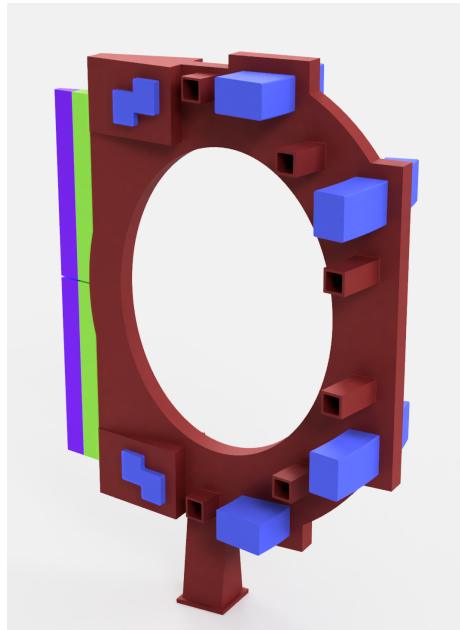


Figure 18: Magnet and structural build of one toroidal section. The CS resin plug is shown in purple, left of the green CS. TF and PF structural supports are shown in maroon, holding the blue PFs. The TF is embedded inside the ovular section of the maroon support structure. Eighteen equivalent toroidal sections encircle the device center-line to form the full CENTAUR build.

COMSOL is used to assess the Von Mises stress on the magnet system components. For the purpose of this analysis, two loading conditions are considered. In the first, the central solenoid is at its maximum current, and in the second, the central solenoid has zero current. For both conditions, the toroidal field coils, poloidal field coils, and plasma have maximum current. In the COMSOL model, the plasma is represented as a single filament at the magnetic axis. These two loading conditions are expected to create the maximum stresses on the magnets and structural components.

Results from these COMSOL simulations are depicted in Figure 19. Between both loading conditions, the maximum stresses on the toroidal field coils, central solenoid, and poloidal field coils are 415 MPa, 332 MPa, and 458 MPa, respectively. HTS critical current is not expected to degrade until 650 MPa [69], giving about a 40% minimum margin of safety on all HTS components.

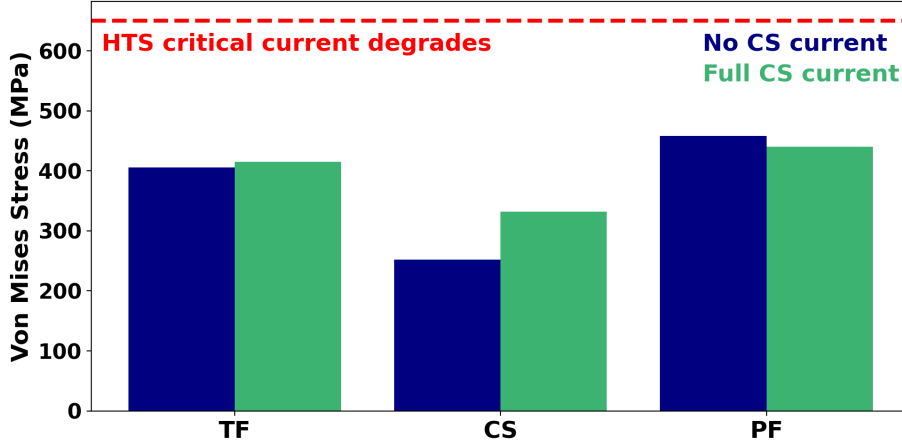


Figure 19: Von Mises stress on the toroidal field coils, central solenoid, and poloidal field coils for no central solenoid current and maximum central solenoid current.

Preliminary COMSOL simulations also suggest that the peak loads on the toroidal field coil structure are below the 1400 MPa yield stress of Nitronic 40 for both loading conditions. Future solid mechanics simulations will be used to further optimize the mechanical structure and validate stress predictions.

#### 4.5 Vacuum vessel stresses from disruption-induced current quenches

TokaMaker is used to simulate current quenches (CQ) from VDE-induced disruptions and from symmetric disruptions. VDE simulations are described in section 2. To simulate VDE disruptions, the coil currents are turned off when the plasma touches the limiter, and the consequent current-quench evolution is simulated in TokaMaker with fixed current distribution. For symmetric disruptions, the coil currents are turned off from the base equilibrium instead. In both cases, a fast CQ time of 3 ms is assumed using the ITPA disruptions database scaling [70]. As the plasma evolves, the induced current density in the vacuum vessel (VV) and the resulting  $\mathbf{J} \times \mathbf{B}$  forces are found as a function of time. The peak force on the VV is then used to calculate the maximum stress on the VV.

The  $\mathbf{J} \times \mathbf{B}$  forces are applied to a realistic 3D VV geometry shown in 20 a) to calculate electromagnetic stresses, shown in 20 b) and 20 c). The maximum stresses, located in the outboard side marked "max", are 249 MPa for VDE

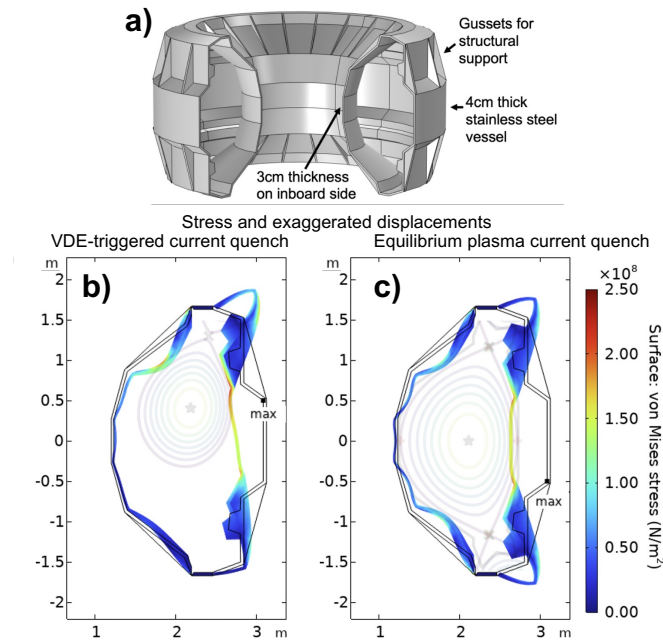


Figure 20: Current quench stresses on the vacuum vessel from VDE and vertically symmetric disruptions. a) shows the vacuum vessel design including gussets for structural support. b) shows the electromagnetic stress on the vacuum vessel from a VDE, and c) is the stress from a symmetric current quench. The Tokamaker equilibria before a disruption are shown in a lighter shade.

CQs and 230 MPa for symmetric CQs. According to experimental steel fatigue studies [71], this results in 100,000 disruptions and 230,000 disruptions before VV structural failure, respectively. Therefore, the VV is unlikely to fail from disruption electromagnetic forces within the design lifetime.

However, for added safety, this analysis led to the addition of gussets to the corners of the VV, which improve VV strength and are thin enough that they don't significantly affect the blanket's ability to shield neutrons. Further fidelity can be achieved by simulating eddy currents in a complete 3D VV geometry, including ports and other structures [72].

## 5 Neutronics Analysis

Comprehensive lifetime analysis was completed using the open-source Monte Carlo neutron simulation code OpenMC [73]. As design points were iterated, a workflow was developed that allows transforming geometric parameters in TokaMaker to OpenMC objects. The neutron source was set as the plasma, based on the core and power team design points, with corresponding neutron outputs that were propagated throughout the whole device. As successive plasma designs were generated in TokaMaker, they were implemented via a framework directly into OpenMC modeling to create a forward feedback loop for the overall design.

### 5.1 Lifetime design goals

The constraining design goals for neutronics analysis are that the device must survive neutron damage from the fluence of 3000 full-power DT pulses and that the superconducting magnets remain below 33 K, so that they avoid quenching during each 10-second pulse. The pulse number is set from the outset, and the 33 K limit is set by considering the critical current and magnetic field constraints set by the magnet team and based on empirical studies of HTS (as noted in section 4.1) [64, 74].

Our simulations validate the general assumptions on neutron activity in fusion devices. Generally, fusion power plant designs such as MANTA [8] and ARC [75] are thought to be limited by neutron damage, or displacement per atom (DPA), rather than nuclear heating. This is due to the bulk of the heat deposition being into the blanket layer, rather than in and around the HTS magnets. Also, power plants are designed to survive across much longer time scales, with much higher neutron fluences. However, in test facilities such as CENTAUR and SPARC [76], which operate shorter pulses with less cumulative neutron flux, the key limiting factor is neutron heating rather than DPA. This ultimately is a critical factor in the design process, since the inboard build required more significant heat shielding than originally planned for. Our modeling supports this outlook, and in the final CENTAUR design all HTS device components are predicted to survive over 10 times the 3000 pulse limit considering solely the DPA. This corresponds to  $3 \times 10^{22}$  neutrons/m<sup>2</sup>.

## 5.2 Radial build and shielding thickness

Given that the primary concern is heat shielding, a variety of materials are tested in the OpenMC workflow to determine the best choice for CENTAUR. A set of fusion power and plasma shapes are taken and used to run identical high-fidelity simulations ( $10^7$  particles) of different materials. The best materials tested are shown in table 5 compared with the HTS heating resulting from the absence of shielding material.

Shielding Material	Percent of Vacuum Heating
B <sub>4</sub> C	42.2%
WC	58.5%
HDPE	73.5%

Table 5: Comparison of shielding materials used to protect the HTS magnets from quenching. HDPE is high-density polyethylene.

Considering the maximum heating reduction provided by B<sub>4</sub>C and its planned use in other tokamak designs [77], the decisions on shielding thickness and placements are completed using only B<sub>4</sub>C. Iterations between shielding width and fusion output produce a satisfactory operating point for core performance without quenching the magnets via neutron heating. This design point is one of the key constraining factors on the radial build of CENTAUR, seen in figure 21.

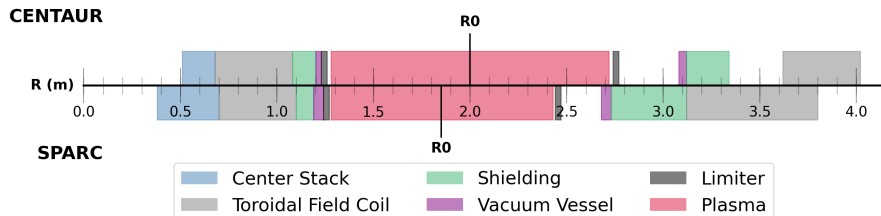


Figure 21: CENTAUR radial build compared to SPARC[78] at the midplane of both devices.

Note that this design is not actively cooled during the shots, so the shielding and operating point is conservative and could be improved given modeling and inclusion of active cooling. While the plasma is considerably larger than SPARC radially, the maximum fusion power for CENTAUR is 40 MW while SPARC is planning on fusion power of around 140 MW.

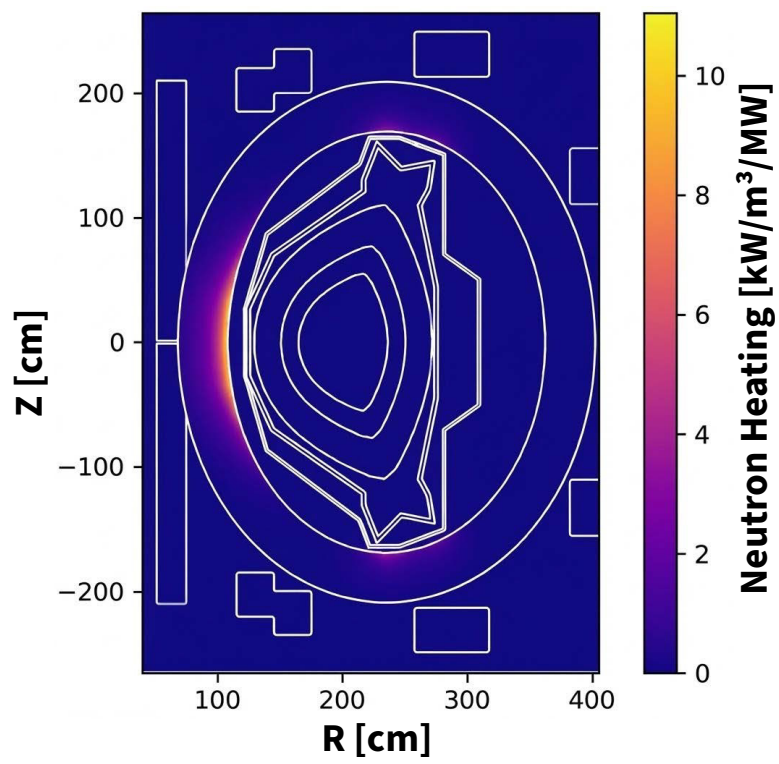


Figure 22: Representative OpenMC Monte Carlo neutron heating simulation using 12 cm of  $B_4C$  shielding. The bulk of the heating is concentrated at the inboard midplane.

During the modeling process, a method was developed to scope out the operating regime in terms of initial temperature, fusion power, and final temperature. Since the neutron heating is concentrated at the inboard mid plane, numerous OpenMC simulations are run to relate fusion power to local volumetric heating ( $\text{kW}/\text{m}^3/\text{MW}$ ). For example, an OpenMC simulation of the design point with 12 cm of  $B_4C$  can be found in figure 22. Then, the specific heat and density of HTS is used to convert the volumetric heating into a change in temperature. In figure 23, the operating point can be seen analyzed with this method, and is below the 33 K temperature limit at which the HTS magnets would quench from heating during operation. This is calculated based on an initial HTS temperature of 8 K with 12 cm of  $B_4C$  and a plasma flat top of 10 seconds.

Considering the two main lifetime limitations from neutrons, DPA and heating, this modeling provides confidence that CENTAUR will meet its neutronics design goals. The DPA modeling shows the HTS will survive well beyond the 3000 DT pulse limit and the heating model shows the HTS will survive the neutron heating over the course of each shot.

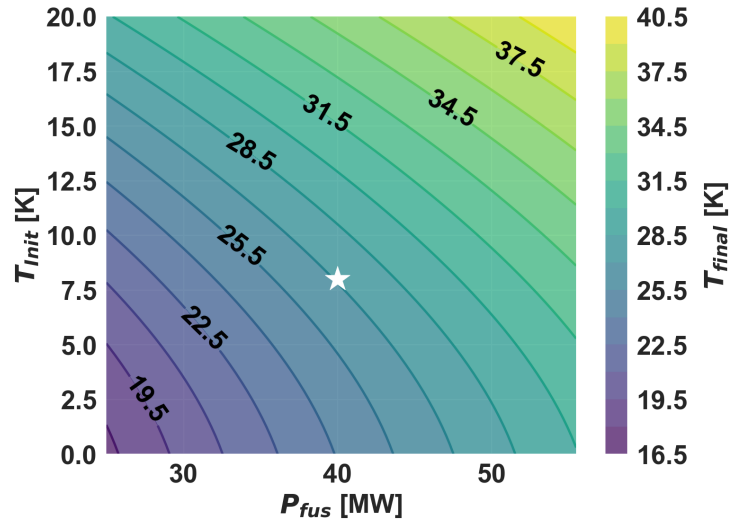


Figure 23: HTS magnet neutron heating over a 10-second shot. The star represents the CENTAUR operating point: initial HTS temperature of 8K, 12 cm of  $B_4C$  shielding, and a 10 second flat top at 40 MW  $P_{fus}$  with final HTS temperature below 33K.

## 6 Economic Analysis

Economic modeling is a critical piece of the design process for FPPs. CENTAUR is constrained to remain within a \$2B overnight cost target and maintain ra-

radioactive material compliance for on-site tritium inventory, in line with current restrictions on particle accelerators[79]. The costing model uses integrated system pricing based on materials and fabrication costs that adjust to the geometric and performance characteristics of the designed reactor similar to the MANTA costing model[8]. CENTAUR achieves a total overnight cost of  $\$1.6\text{B} \pm 0.2\text{B}$  based on the costing model developed in this work, maintaining the initial goal of a maximum budget of  $\$2\text{B}$  with a cost breakdown of 95% direct reactor costs and 5% indirect costs. Direct costs refer to systems that are directly involved in or necessary for the confinement and performance of the plasma while indirect costs are all systems that are needed to enable the direct cost systems or that manage and maintain the device.

## 6.1 Device Costs

Direct device costs constitute the majority of the total cost and are most significantly driven by the TF, PF, and CS magnet systems. Magnet pricing is calculated using the geometry of the TF and PF coils and the total length of HTS tape ( $606\text{km} \pm 90\text{km}$ ). The uncertainty calculation of the magnet systems is highly dependent on the price of HTS, which is difficult to determine given the quantity of HTS needed is not well documented at scale[80]. Sensitivity analysis reveals that the PF coil system is the most affected by variation in the HTS price followed by the CS and TF magnets. The sensitivity to the price of HTS per kA-m is  $\$15.2\text{M}$  for the entire device split between  $\$3.7\text{M}$  for the TF system,  $\$7.5\text{M}$  for the PF system, and  $\$4.1\text{M}$  for the CS system. Figure 24 illustrates how HTS costs dominate the cost of all magnet systems and are the most significant line items of the design.

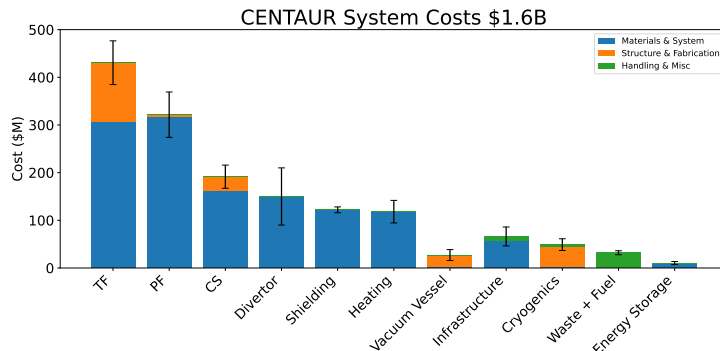


Figure 24: Total cost breakdown of CENTAUR by system.

Structural and fabrication costs are also significant factors in the TF, CS, vacuum vessel, and cryogenics systems. While structural components are not as variable, fabrication costs are the second most variable cost uncertainty after HTS tape. Fabrication costs affect the vacuum vessel costs most and are a significant source of uncertainty due to the lack of public quotes for other similar

devices. Calculations for the overall cost of the vacuum vessel were linearly scaled based on the volume difference between CENTAUR and ITER [81]. Additionally, infrastructure costs are significantly higher compared to MANTA [8] despite the omission of an electricity conversion plant in CENTAUR’s design. This difference is due in large part to additional consideration of the location and construction costs of an operational site using high density concrete for neutron shielding of personnel and the public, though local legal restrictions on radiation sources could diminish construction costs significantly depending on the location site. Furthermore, land, electrical infrastructure, and construction costs were also estimated assuming a 0.25 km<sup>2</sup> campus within Claiborne, MS due to its proximity to the Grand Gulf Nuclear station and available electrical grid infrastructure. The location of the cost estimates was chosen only as an example case study and is not intended as an endorsement of the placement of a device like CENTAUR.

### 6.1.1 Tritium Management

The time evolution of tritium inventories within the fuel cycle was modeled using a system-level simulation implemented in Python, following the residence time method formalism established by Meschini [82]. The computational framework tracks tritium mass across ten coupled components: the primary storage system, tritium extraction system, first wall, divertor, heat exchanger, detritiation system, vacuum pumps, fuel cleanup system, isotope separation system, and membrane separation unit. Each component is characterized by a residence time  $\tau$  that governs the rate of tritium throughput. The tritium mass balance for each component obeys the differential equation

$$\frac{dI_i}{dt} = \sum_j \frac{I_j f_{j \rightarrow i}}{\tau_j} - \frac{(1 + \epsilon)I_i}{\tau_i} - \lambda I_i, \quad (1)$$

where  $I_i$  denotes the tritium inventory in component  $i$ , the coefficients  $f_{j \rightarrow i}$  represent fractional flows between components,  $\epsilon = 10^{-4}$  accounts for non-radioactive losses and  $\lambda = 1.73 \times 10^{-9} \text{ s}^{-1}$  is the radioactive decay constant corresponding to the 12.33 year tritium half-life. The coupled system of ordinary differential equations is integrated using the backward differentiation formula method, which provides numerical stability for the stiff dynamics arising from residence times that span several orders of magnitude, ranging from approximately 100 seconds in the membrane separation unit to 24 hours in the tritium extraction system. The baseline simulation assumes a tritium burn rate of  $\dot{N} = 9.3 \times 10^{-7} \text{ kg/s}$  and a tritium burn efficiency of 2%, with component processing efficiencies uniformly set to 95% [82]. This implementation models only the inner fuel cycle dynamics and omits the breeding blanket, as the present analysis concerns fuel processing and recirculation pathways rather than tritium breeding.

## 6.2 Costing Model Validation

The CENTAUR costing model calculates costs for all the items listed in table 8 by system. Table 6 shows the comparison of the CENTAUR costing model overnight cost predictions against the ARIES [83], and Sheffield [84] costing model for CENTAUR and SPARC designs. The CENTAUR costing model is more consistent with the ARIES model for CENTAUR’s design, though it overpredicts the cost of SPARC in comparison. This difference in cost is due to both model’s overemphasis on the cost of the poloidal field coils. Both models price the PF system differently than the toroidal field coils for the same field strength. illustrates this lopsided costing for SPARC. Despite the smaller discrepancy for SPARC, overall agreement between all costing models gives confidence to the overall \$1.6B estimate of the entire device.

Model	CENTAUR	SPARC
CENTAUR	\$1.6B	\$1.7B
ARIES[83]	\$1.8B	\$1.6B
Sheffield[84]	\$2.1B	\$1.8B

Table 6: This table shows the overnight costs of CENTAUR and SPARC using the CENTAUR, ARIES, and Sheffield costing models.

Economic analysis of CENTUAR shows the design to be cost effective and within initial goal of  $\leq$ \$2B overnight cost. The economic analysis using the CENTAUR costing model shows agreement with other historic costing models such as the ARIES and Sheffield models. Furthermore, the CENTAUR design costing model demonstrate that negative triangularity is not a cost prohibitive design choice for construction and operation. The success in economic projection is due in large part to the co-design process since the CENTAUR model allows for rapid iteration and individual system pricing that can inform system design.

## 7 Conclusion

CENTAUR offers a novel break even fusion device with a robust power handling scheme, largely due to advantages from strong negative triangularity plasma shaping. High-field from superconducting magnets ensures sufficient confinement for  $Q > 1$  operation, outside of H-mode and ELM-free. The large wetted surface and high radiative fraction of the NT divertor region allows for simple divertor geometry and a high margin of safety for plasma facing components. The HTS magnet systems produce a high toroidal field and sufficient flux swing in a compact design while remaining below HTS critical current limits. The neutronics analysis confirms the viability of the device lifetime constraints and the necessary shielding to prevent unacceptable heat rise in the HTS magnets. Further, costing analysis shows that this device can be constructed, operated, and

Material	Cost per unit [\$ (USD)]	System
REBCO (HTS)	40 [Estimate]/kAm	TF,PF,CS
nitronic 60 (steel)	25/kg	TF,PF,CS
Tungsten Carbide	85/kg	Shielding
Liquid He	30/L	Cryo
Tritium	30,000/g	Fueling
Copper	8/kg	Heating, Cryo, Infrastr.
Deuterium	11/g	Fueling
Chromium-Vanadium	43/kg	Vacuum Vessel
High density Concrete	37.4/ft <sup>3</sup>	Infrastr.

Table 7: Table of materials cost used for pricing of CENTAUR.

decommissioned within the budget limitations prescribed for the design study. This design study shows that CENTAUR provides the necessary stepping stone between current-day tokamaks and a fusion pilot plant by demonstrating the negative triangularity operational scheme in  $Q > 1$  DT plasma conditions. The self-consistent analysis presented demonstrates that CENTAUR is designed to achieve scientific gain of 1.3 at an overnight cost under \$2B while employing available technologies and traditional heat exhaust divertor schemes

Future work would most likely include a continued optimization of the operating scenario to extract maximal plasma performance. Further, the inclusion of self-consistent ion cyclotron resonant heating models would improve understanding of our expected core scenario. One of the principal areas of uncertainty in this design is magnet heating due to neutron fluence. A follow-up study to determine the effects of active cooling on superconducting TF coils would be of high value.

## Acknowledgements

The authors are grateful to all other course members of Columbia APPH 9142, including Princeton students who participated through the Inter-University Engineering Doctoral Consortium, and for the expert advice of Dr. Michael Bergmann. This work was supported in part by Columbia University, US DOE Grants DE-SC0024898, DE-SC0022270 and DE-SC0022272, US DOE contract DE-AC52 07NA27344, and NSF award 2401039.

Item	Cost (\$M)	System & Category	Costing Method
TF HTS tape	148	TF	Materials/System
TF structural supports	125	TF	Structure & Fabrication
TF resistive Leads	158	TF	Materials/System
PF HTS tape	302	PF	Materials/System
PF structural supports	4	PF	Structure & Fabrication
PF resistive Leads	16	PF	Materials/Systems
CS HTS tape	162	CS	Materials/System
CS structural supports	30	CS	Structure & Fabrication
Divertor materials	150	Divertor	Materials/System
Divertor coolants	<1	Divertor	Materials/System
ICRH	118	Heating	Materials/System
1st and 2nd wall	6	VV	Materials/System
VV fabrication	86	VV	Structure & Fabrication
Land	<1	Infrastructure	Handling & Misc.
Electrical substation	4	Infrastructure	Handling & Misc.
Electrical power lines	5	Infrastructure	Handling & Misc.
Plant building materials	56	Infrastructure	Materials/System
Magnet Coolant costs	3	Cryo	Materials/System
Cryostat structure	41	Cryo	Structure & Fabrication
Coolant recycling	5	Cryo	Handling & Misc.
Neutron Shielding	122	Shielding	Materials/System
Tritium Inventory	<1	Fueling	Materials/System
Tritium Handling	31	Fueling	Handling & Misc.
Energy Storage batteries	10	Energy Storage	Materials/System

Table 8: This table shows every cost calculated for CENTAUR using its costing model.

## References

- [1] F. Scotti et al. “High performance power handling in the absence of an H-mode edge in negative triangularity DIII-D plasmas”. en. In: *Nuclear Fusion* 64.9 (Sept. 2024), p. 094001. ISSN: 0029-5515. DOI: 10.1088/1741-4326/ad5f41. URL: <https://doi.org/10.1088/1741-4326/ad5f41> (visited on 03/31/2026).
- [2] A. O. Nelson et al. “Robust Avoidance of Edge-Localized Modes alongside Gradient Formation in the Negative Triangularity Tokamak Edge”. en. In: *Physical Review Letters* 131.19 (Nov. 2023), p. 195101. ISSN: 0031-9007, 1079-7114. DOI: 10.1103/PhysRevLett.131.195101. URL: <https://link.aps.org/doi/10.1103/PhysRevLett.131.195101> (visited on 05/02/2026).
- [3] M. E. Austin et al. “Diverted Negative Triangularity Plasmas on DIII-D: The Benefit of High Confinement without the Liability of an Edge Pedestal”. In: *Nuclear Fusion* 61.11 (2021), p. 116016. DOI: 10.1088/1741-4326/ac1f90. URL: <https://doi.org/10.1088/1741-4326/ac1f90>.
- [4] A. Q. Kuang et al. “Divertor heat flux challenge and mitigation in SPARC”. en. In: *Journal of Plasma Physics* 86.5 (Oct. 2020), p. 865860505. ISSN: 0022-3778, 1469-7807. DOI: 10.1017/S0022377820001117. URL: <https://www.cambridge.org/core/journals/journal-of-plasma-physics/article/divertor-heat-flux-challenge-and-mitigation-in-sparc/A25A8CFADDBA33AD9AAC18F24E40A18E> (visited on 03/27/2026).
- [5] S.Yu. Medvedev et al. “The negative triangularity tokamak: stability limits and prospects as a fusion energy system”. en. In: *Nuclear Fusion* 55.6 (May 2015), p. 063013. ISSN: 0029-5515. DOI: 10.1088/0029-5515/55/6/063013. URL: <https://doi.org/10.1088/0029-5515/55/6/063013> (visited on 03/05/2026).
- [6] T. Slendebroek et al. “Exploring the fusion power plant design space: comparative analysis of positive and negative triangularity tokamaks through optimization”. In: *Nuclear Fusion* 66.2 (2026). DOI: 10.1088/1741-4326/ae27e6. URL: <https://doi.org/10.1088/1741-4326/ae27e6>.
- [7] S. Guizzo et al. “Electromagnetic system conceptual design for a negative triangularity tokamak”. In: *Fusion Engineering and Design* 219 (2025), p. 115257. ISSN: 0920-3796. DOI: <https://doi.org/10.1016/j.fusengdes.2025.115257>. URL: <https://www.sciencedirect.com/science/article/pii/S0920379625004533>.
- [8] The MANTA Collaboration et al. “MANTA: a negative-triangularity NASEM-compliant fusion pilot plant”. en. In: *Plasma Physics and Controlled Fusion* 66.10 (Oct. 2024), p. 105006. ISSN: 0741-3335, 1361-6587. DOI: 10.1088/1361-6587/ad6708. URL: <https://iopscience.iop.org/article/10.1088/1361-6587/ad6708> (visited on 01/14/2026).

- [9] B.N. Sorbom et al. “ARC: A Compact, High-Field, Fusion Nuclear Science Facility and Demonstration Power Plant with Demountable Magnets”. In: *Fusion Engineering and Design* 100 (Nov. 2015), pp. 378–405. ISSN: 09203796. DOI: 10.1016/j.fusengdes.2015.07.008. (Visited on 02/18/2024).
- [10] A.O. Nelson et al. “First access to ELM-free negative triangularity at low aspect ratio”. en. In: *Nuclear Fusion* 64.12 (Oct. 2024), p. 124004. ISSN: 0029-5515. DOI: 10.1088/1741-4326/ad89db. URL: <https://doi.org/10.1088/1741-4326/ad89db> (visited on 02/10/2026).
- [11] P. Lunia, A. O. Nelson, and C. Paz-Soldan. *Energy Confinement Time Scaling Law Derived from Paz-Soldan NF 2024*. 2025. arXiv: 2509.04279 [physics.plasm-ph]. URL: <https://arxiv.org/abs/2509.04279>.
- [12] C. Hansen et al. “TokaMaker: An open-source time-dependent Grad-Shafranov tool for the design and modeling of axisymmetric fusion devices”. In: *Computer Physics Communications* 298 (May 2024), p. 109111. ISSN: 0010-4655. DOI: 10.1016/j.cpc.2024.109111. URL: <http://dx.doi.org/10.1016/j.cpc.2024.109111>.
- [13] A. Marinoni et al. “H-Mode Grade Confinement in L-mode Edge Plasmas at Negative Triangularity on DIII-D”. In: *Physics of Plasmas* 26.4 (Apr. 2019), p. 042515. ISSN: 1070-664X. DOI: 10.1063/1.5091802. eprint: [https://pubs.aip.org/aip/pop/article-pdf/doi/10.1063/1.5091802/19778787/042515\\_1\\_online.pdf](https://pubs.aip.org/aip/pop/article-pdf/doi/10.1063/1.5091802/19778787/042515_1_online.pdf). URL: <https://doi.org/10.1063/1.5091802>.
- [14] M. E. Austin et al. “Achievement of Reactor-Relevant Performance in Negative Triangularity Shape in the DIII-D Tokamak”. In: *Phys. Rev. Lett.* 122 (11 Mar. 2019), p. 115001. DOI: 10.1103/PhysRevLett.122.115001. URL: <https://link.aps.org/doi/10.1103/PhysRevLett.122.115001>.
- [15] Tom Body et al. *cfs-energy/cfspopcon: v7.0.2*. 2024.
- [16] W.A. Houlberg, S.E. Attenberger, and L.M. Hively. “Contour Analysis of Fusion Reactor Plasma Performance”. In: *Nuclear Fusion* 22.7 (July 1982), p. 935. DOI: 10.1088/0029-5515/22/7/006. URL: <https://doi.org/10.1088/0029-5515/22/7/006>.
- [17] Gregorij V Pereverzev and e PN Yushmanov. *ASTRA. Automated System for TRansport Analysis in a tokamak*. 2002.
- [18] G. M. Staebler, J. E. Kinsey, and R. E. Waltz. “Gyro-Landau Fluid Equations for Trapped and Passing Particles”. In: *Physics of Plasmas* 12.10 (Oct. 2005), p. 102508. ISSN: 1070-664X. DOI: 10.1063/1.2044587. eprint: [https://pubs.aip.org/aip/pop/article-pdf/doi/10.1063/1.2044587/14688354/102508\\_1\\_online.pdf](https://pubs.aip.org/aip/pop/article-pdf/doi/10.1063/1.2044587/14688354/102508_1_online.pdf). URL: <https://doi.org/10.1063/1.2044587>.

- [19] C. Hansen et al. “TokaMaker: An Open-Source Time-Dependent Grad-Shafranov Tool for the Design and Modeling of Axisymmetric Fusion Devices”. In: *Computer Physics Communications* 298 (2024), p. 109111. ISSN: 0010-4655. DOI: 10.1016/j.cpc.2024.109111. URL: <https://www.sciencedirect.com/science/article/pii/S0010465524000341>.
- [20] T. D. Rognlien et al. “A Fully Implicit, Time Dependent 2-D Fluid Code for Modeling Tokamak Edge Plasmas”. In: *Journal of Nuclear Materials. Plasma-Surface Interactions in Controlled Fusion Devices* 196–198 (Dec. 1992), pp. 347–351. ISSN: 0022-3115. DOI: 10.1016/S0022-3115(06)80058-9. URL: <https://www.sciencedirect.com/science/article/pii/S0022311506800589> (visited on 04/06/2026).
- [21] R. L. Miller et al. “Stable Equilibria for Bootstrap-Current-Driven Low Aspect Ratio Tokamaks”. In: *Physics of Plasmas* 4.4 (Apr. 1997), pp. 1062–1068. ISSN: 1070-664X. DOI: 10.1063/1.872193. eprint: [https://pubs.aip.org/aip/pop/article-pdf/4/4/1062/19079719/1062\\_1\\_online.pdf](https://pubs.aip.org/aip/pop/article-pdf/4/4/1062/19079719/1062_1_online.pdf). URL: <https://doi.org/10.1063/1.872193>.
- [22] K E Thome et al. “Overview of Results from the 2023 DIII-D Negative Triangularity Campaign”. In: *Plasma Physics and Controlled Fusion* 66.10 (Sept. 2024), p. 105018. DOI: 10.1088/1361-6587/ad6f40. URL: <https://doi.org/10.1088/1361-6587/ad6f40>.
- [23] A O Nelson et al. “Characterization of the ELM-free Negative Triangularity Edge on DIII-D”. In: *Plasma Physics and Controlled Fusion* 66.10 (Sept. 2024), p. 105014. ISSN: 0741-3335. DOI: 10.1088/1361-6587/ad6a83. URL: <https://doi.org/10.1088/1361-6587/ad6a83> (visited on 02/13/2026).
- [24] C. Paz-Soldan et al. “Simultaneous access to high normalized density, current, pressure, and confinement in strongly-shaped diverted negative triangularity plasmas”. In: *Nuclear Fusion* 64.9 (Aug. 2024), p. 094002. ISSN: 0029-5515. DOI: 10.1088/1741-4326/ad69a4. URL: <https://doi.org/10.1088/1741-4326/ad69a4> (visited on 04/03/2026).
- [25] G. Pereverzev and P. N. Yushmanov. “ASTRA Automated System for TRansport Analysis in a Tokamak”. In: *Max Planck Institute for Plasma Physics, Garching, Germany* (2002). URL: [https://pure.mpg.de/rest/items/item\\_2138238/component/file\\_2138237/content](https://pure.mpg.de/rest/items/item_2138238/component/file_2138237/content).
- [26] E. Fable et al. “Novel free-boundary equilibrium and transport solver with theory-based models and its validation against ASDEX Upgrade current ramp scenarios”. In: *Plasma Phys. Control. Fusion* 55.12 (2013), p. 124028. DOI: 10.1088/0741-3335/55/12/124028. URL: <https://dx.doi.org/10.1088/0741-3335/55/12/124028>.
- [27] G. M. Staebler, J. E. Kinsey, and R. E. Waltz. “A theory-based transport model with comprehensive physics”. In: *Physics of Plasmas* 14.5 (2007), p. 055909. ISSN: 1070-664X. DOI: 10.1063/1.2436852. URL: <https://doi.org/10.1063/1.2436852>.

- [28] J McClenaghan et al. “Examining transport and integrated modeling predictive capabilities for negative-triangularity scenarios”. In: *Plasma Physics and Controlled Fusion* 66.11 (2024), p. 115008.
- [29] L Aucone et al. “Experiments and Modelling of Negative Triangularity ASDEX Upgrade Plasmas in View of DTT Scenarios”. In: *Plasma Physics and Controlled Fusion* 66.7 (May 2024), p. 075013. DOI: 10.1088/1361-6587/ad4d1c. URL: <https://doi.org/10.1088/1361-6587/ad4d1c>.
- [30] H S Wilson et al. “Characterizing the Negative Triangularity Reactor Core Operating Space with Integrated Modeling”. In: *Plasma Physics and Controlled Fusion* 67.1 (Jan. 31, 2025), p. 015026. ISSN: 0741-3335, 1361-6587. DOI: 10.1088/1361-6587/ad9be5. URL: <https://iopscience.iop.org/article/10.1088/1361-6587/ad9be5> (visited on 03/06/2026).
- [31] A. Mariani et al. “First-Principle Based Predictions of the Effects of Negative Triangularity on DTT Scenarios”. In: *Nuclear Fusion* 64.4 (Feb. 2024), p. 046018. DOI: 10.1088/1741-4326/ad2abc. URL: <https://doi.org/10.1088/1741-4326/ad2abc>.
- [32] D Fajardo et al. “Analytical Model for the Combined Effects of Rotation and Collisionality on Neoclassical Impurity Transport”. In: *Plasma Physics and Controlled Fusion* 65.3 (Feb. 2023), p. 035021. ISSN: 0741-3335. DOI: 10.1088/1361-6587/acb0fc. URL: <https://doi.org/10.1088/1361-6587/acb0fc> (visited on 04/27/2026).
- [33] S. Guizzo et al. *Assessment of vertical stability for negative triangularity pilot plants*. en. arXiv:2401.15217 [physics]. Jan. 2024. DOI: 10.48550/arXiv.2401.15217. URL: <http://arxiv.org/abs/2401.15217> (visited on 03/23/2026).
- [34] A.O. Nelson et al. “Implications of vertical stability control on the SPARC tokamak”. en. In: *Nuclear Fusion* 64.8 (June 2024), p. 086040. ISSN: 0029-5515. DOI: 10.1088/1741-4326/ad58f6. URL: <https://doi.org/10.1088/1741-4326/ad58f6> (visited on 04/01/2026).
- [35] Charlie Sanabria et al. “Development of a high current density, high temperature superconducting cable for pulsed magnets”. en. In: *Superconductor Science and Technology* 37.11 (Nov. 2024), p. 115010. ISSN: 0953-2048, 1361-6668. DOI: 10.1088/1361-6668/ad7efc. URL: <https://iopscience.iop.org/article/10.1088/1361-6668/ad7efc> (visited on 01/14/2026).
- [36] K. Krieger et al. “Scrape-off layer and divertor physics: Chapter 5 of the special issue: on the path to tokamak burning plasma operation”. In: *Nuclear Fusion* 65.4 (Mar. 2025), p. 043001. DOI: 10.1088/1741-4326/adaf42. URL: <https://doi.org/10.1088/1741-4326/adaf42>.
- [37] U.S. Department of Energy. *Report on Science Challenges and Research Opportunities in Plasma Materials Interactions*. Technical Report. Washington, DC, USA: U.S. Department of Energy, 2015.

- [38] P. C. Stangeby. *The Plasma Boundary of Magnetic Fusion Devices*. Institute of Physics Publishing, 2000.
- [39] A. Loarte et al. “Plasma Detachment in JET Mark I Divertor Experiments”. In: *Nuclear Fusion* 38.3 (Mar. 1998), p. 331. ISSN: 0029-5515. DOI: 10.1088/0029-5515/38/3/303. (Visited on 04/03/2026).
- [40] A. W. Leonard. “Plasma detachment in divertor tokamaks”. In: *Plasma Physics and Controlled Fusion* (2018). DOI: 10.1088/1361-6587/aaa7a9.
- [41] S. I. Krasheninnikov. “Physics of ultimate detachment of a tokamak divertor plasma”. In: *Journal of Plasma Physics* (2017).
- [42] N. Asakura, K. Hoshino, et al. “Recent progress of plasma exhaust concepts and divertor designs for tokamak DEMO reactors”. In: *Nuclear Materials and Energy* (2023). DOI: 10.1016/j.nme.2023.101446.
- [43] G. Federici and C. Skinner. “Plasma–material interactions in current tokamaks and their implications for next step devices”. In: *Journal of Nuclear Materials* (2001). Review of underlying physical processes and experimental database.
- [44] R. A. Pitts et al. “Chapter 5: Physics of the ITER divertor”. In: *Nuclear Fusion* 47.6 (2007), S143–S194. DOI: 10.1088/0029-5515/47/6/S05. URL: <https://doi.org/10.1088/0029-5515/47/6/S05>.
- [45] T. Eich et al. “Scaling of the tokamak near the scrape-off layer H-mode power width and implications for ITER”. In: *Nuclear Fusion* 53.9 (2013), p. 093031. DOI: 10.1088/0029-5515/53/9/093031. URL: <https://doi.org/10.1088/0029-5515/53/9/093031>.
- [46] A. Scarabosio et al. “Scaling of the tokamak scrape-off layer power fall-off length in L-mode plasmas”. In: *Nuclear Fusion* 53.11 (2013), p. 113002. DOI: 10.1088/0029-5515/53/11/113002. URL: <https://doi.org/10.1088/0029-5515/53/11/113002>.
- [47] T. D. Rognlien and M. E. Rensink. *Users manual for the UEDGE edge-plasma transport code*. LLNL Report, 2023. URL: <https://github.com/llnl/UEDGE/releases/tag/v8.1.1-patch.0>.
- [48] C. Hansen et al. “TokaMaker: An open-source time-dependent Grad-Shafranov tool for the design and modeling of axisymmetric fusion devices”. en. In: *Computer Physics Communications* 298 (May 2024), p. 109111. ISSN: 00104655. DOI: 10.1016/j.cpc.2024.109111. URL: <https://linkinghub.elsevier.com/retrieve/pii/S0010465524000341> (visited on 01/16/2026).
- [49] Yu. L. Igitkhanov. “Impurity Transport at Arbitrary Densities in the Divertor Plasma”. In: *Contributions to Plasma Physics* 28.4-5 (1988), pp. 477–482. DOI: <https://doi.org/10.1002/ctpp.2150280435>. eprint: <https://onlinelibrary.wiley.com/doi/pdf/10.1002/ctpp.2150280435>. URL: <https://onlinelibrary.wiley.com/doi/abs/10.1002/ctpp.2150280435>.

- [50] F Scotti et al. “Divertor characterization and access to dissipative divertor conditions in negative triangularity discharges in DIII-D”. In: *Plasma Physics and Controlled Fusion* 67.9 (2025), p. 095030. DOI: 10.1088/1361-6587/adf881. URL: <https://doi.org/10.1088/1361-6587/adf881>.
- [51] M.I Guseva et al. “Sputtering of beryllium, tungsten, tungsten oxide and mixed W–C layers by deuterium ions in the near-threshold energy range”. In: *Journal of Nuclear Materials* 266-269 (1999), pp. 222–227. ISSN: 0022-3115. DOI: [https://doi.org/10.1016/S0022-3115\(98\)00819-8](https://doi.org/10.1016/S0022-3115(98)00819-8). URL: <https://www.sciencedirect.com/science/article/pii/S0022311598008198>.
- [52] J.P. Roszell et al. “Deuterium retention in single-crystal tungsten irradiated with 10–500 eV/D+”. In: *Journal of Nuclear Materials* 438 (2013). Proceedings of the 20th International Conference on Plasma-Surface Interactions in Controlled Fusion Devices, S1084–S1087. ISSN: 0022-3115. DOI: <https://doi.org/10.1016/j.jnucmat.2013.01.238>. URL: <https://www.sciencedirect.com/science/article/pii/S0022311513002468>.
- [53] Q. Zhang et al. “Spectroscopic investigation of the tungsten deuteride sputtering in the EAST divertor”. In: *Nuclear Materials and Energy* 33 (2022), p. 101265. ISSN: 2352-1791. DOI: <https://doi.org/10.1016/j.nme.2022.101265>. URL: <https://www.sciencedirect.com/science/article/pii/S2352179122001466>.
- [54] V A Soukhanovskii. “A Review of Radiative Detachment Studies in Tokamak Advanced Magnetic Divertor Configurations”. In: *Plasma Physics and Controlled Fusion* 59.6 (Apr. 2017), p. 064005. ISSN: 0741-3335. DOI: 10.1088/1361-6587/aa6959. (Visited on 04/08/2026).
- [55] Peter C. Stangeby. *The Plasma Boundary of Magnetic Fusion Devices*. Plasma Physics Series. Bristol [ u.a. ]: Institute of Physics Publ, 2000. ISBN: 978-0-7503-0559-4.
- [56] M. Faitsch et al. “Broadening of the Power Fall-off Length in a High Density, High Confinement H-mode Regime in ASDEX Upgrade”. In: *Nuclear Materials and Energy* 26 (Mar. 2021), p. 100890. ISSN: 2352-1791. DOI: 10.1016/j.nme.2020.100890. (Visited on 04/08/2026).
- [57] J. Ren et al. “Experimental Observation of Heat Flux Mitigation during Divertor Detachment in the DIII-D Small Angle Slot Divertor”. In: *Nuclear Materials and Energy* 26 (Mar. 2021), p. 100887. ISSN: 2352-1791. DOI: 10.1016/j.nme.2020.100887. (Visited on 04/08/2026).
- [58] V A Soukhanovskii et al. “Divertor Heat Flux Reduction and Detachment in NSTX”. In: ().
- [59] L. Wang et al. “Integration of Full Divertor Detachment with Improved Core Confinement for Tokamak Fusion Plasmas”. In: *Nature Communications* 12.1 (Mar. 2021), p. 1365. ISSN: 2041-1723. DOI: 10.1038/s41467-021-21645-y. (Visited on 04/08/2026).

- [60] R.A. Pitts et al. “Physics basis for the first ITER tungsten divertor”. en. In: *Nuclear Materials and Energy* 20 (Aug. 2019), p. 100696. ISSN: 23521791. DOI: 10.1016/j.nme.2019.100696. URL: <https://linkinghub.elsevier.com/retrieve/pii/S2352179119300237> (visited on 03/05/2026).
- [61] A. Suslova et al. “Recrystallization and grain growth induced by ELMS-like transient heat loads in deformed tungsten samples”. en. In: *Scientific Reports* 4.1 (Nov. 2014), p. 6845. ISSN: 2045-2322. DOI: 10.1038/srep06845. URL: <https://www.nature.com/articles/srep06845> (visited on 02/16/2026).
- [62] Zachary S. Hartwig et al. “The SPARC Toroidal Field Model Coil Program”. In: *IEEE Transactions on Applied Superconductivity* 34.2 (Mar. 2024), pp. 1–16. ISSN: 1558-2515. DOI: 10.1109/TASC.2023.3332613. URL: <https://ieeexplore.ieee.org/document/10316582/> (visited on 01/14/2026).
- [63] D G Whyte et al. “Experimental Assessment and Model Validation of the SPARC Toroidal Field Model Coil”. en. In: *IEEE TRANSACTIONS ON APPLIED SUPERCONDUCTIVITY* 34.2 (2024).
- [64] A. Molodyk et al. “Development and large volume production of extremely high current density YBa<sub>2</sub>Cu<sub>3</sub>O<sub>7</sub> superconducting wires for fusion”. en. In: *Scientific Reports* 11.1 (Jan. 2021), p. 2084. ISSN: 2045-2322. DOI: 10.1038/s41598-021-81559-z. URL: <https://www.nature.com/articles/s41598-021-81559-z> (visited on 01/14/2026).
- [65] Michael J. Wolf et al. “Critical Current Densities of 482 A/mm<sup>2</sup> in HTS CrossConductors at 4.2 K and 12 T”. en. In: *IEEE Transactions on Applied Superconductivity* 28.4 (June 2018), pp. 1–4. ISSN: 1051-8223, 1558-2515. DOI: 10.1109/TASC.2018.2815767. URL: <https://ieeexplore.ieee.org/document/8316945/> (visited on 02/12/2026).
- [66] J. File, R. G. Mills, and G. V. Sheffield. “Large Superconducting Magnet Designs for Fusion Reactors”. In: *IEEE Transactions on Nuclear Science* 18.4 (Aug. 1971), pp. 277–282. ISSN: 1558-1578. DOI: 10.1109/TNS.1971.4326354. URL: <https://ieeexplore.ieee.org/document/4326354> (visited on 01/14/2026).
- [67] Masayoshi SUGIHARA et al. “Plasma Design Considerations of Near Term Tokamak Fusion Experimental Reactor”. In: *Journal of Nuclear Science and Technology* 19.8 (Aug. 1982). eprint: <https://doi.org/10.1080/18811248.1982.9734193>, pp. 628–637. ISSN: 0022-3131. DOI: 10.1080/18811248.1982.9734193. URL: <https://doi.org/10.1080/18811248.1982.9734193> (visited on 01/14/2026).
- [68] Jim Leuer. *Ramp-Up Flux Consumption of +- Triangularity Plasmas*. Private communication. May 2020.

- [69] Christian Barth, Giorgio Mondonico, and Carmine Senatore. “Electromechanical properties of REBCO coated conductors from various industrial manufacturers at 77 K, self-field and 4.2 K, 19 T”. In: *Superconductor Science and Technology* 28.4 (2015), p. 045011. DOI: 10.1088/0953-2048/28/4/045011.
- [70] N.W. Eidiētis et al. “The ITPA disruption database”. en. In: *Nuclear Fusion* 55.6 (May 2015), p. 063030. ISSN: 0029-5515. DOI: 10.1088/0029-5515/55/6/063030. URL: <https://doi.org/10.1088/0029-5515/55/6/063030> (visited on 01/16/2026).
- [71] K A Mohammad et al. “Fatigue behavior of Austenitic Type 316L Stainless Steel”. en. In: *IOP Conference Series: Materials Science and Engineering* 36 (Sept. 2012), p. 012012. ISSN: 1757-899X. DOI: 10.1088/1757-899X/36/1/012012. URL: <https://iopscience.iop.org/article/10.1088/1757-899X/36/1/012012> (visited on 03/22/2026).
- [72] Christopher Hansen et al. “ThinCurr: An open-source 3D thin-wall eddy current modeling code for the analysis of large-scale systems of conducting structures”. In: *Computer Physics Communications* 315 (2025), p. 109713. ISSN: 0010-4655. DOI: <https://doi.org/10.1016/j.cpc.2025.109713>. URL: <https://www.sciencedirect.com/science/article/pii/S0010465525002152>.
- [73] Paul K. Romano et al. “OpenMC: A state-of-the-art Monte Carlo code for research and development”. In: *Annals of Nuclear Energy* 82 (2015), pp. 90–97. DOI: 10.1016/j.anucene.2014.07.048. URL: <https://doi.org/10.1016/j.anucene.2014.07.048>.
- [74] D. X. Fischer et al. “The effect of fast neutron irradiation on the superconducting properties of REBCO coated conductors with and without artificial pinning centers”. In: *Superconductor Science and Technology* 31.4 (2018), p. 044006. DOI: 10.1088/1361-6668/aaadf2.
- [75] B. N. Sorbom et al. “ARC: A compact, high-field, fusion nuclear science facility and demonstration power plant with demountable magnets”. In: *Fusion Engineering and Design* 100 (2015), pp. 378–405. DOI: 10.1016/j.fusengdes.2015.07.008.
- [76] A. J. Creely et al. “Overview of the SPARC tokamak”. In: *Journal of Plasma Physics* 86.5 (2020), p. 865860502. DOI: 10.1017/S0022377820001257.
- [77] X. Wang et al. “An OpenMC model of the SPARC tokamak for the diagnostic scoping studies”. In: *Fusion Engineering and Design* 221 (2025), p. 115390. ISSN: 0920-3796. DOI: <https://doi.org/10.1016/j.fusengdes.2025.115390>. URL: <https://www.sciencedirect.com/science/article/pii/S0920379625005861>.

- [78] P. Rodriguez-Fernandez et al. “Overview of the SPARC Physics Basis towards the Exploration of Burning-Plasma Regimes in High-Field, Compact Tokamaks”. In: *Nuclear Fusion* 62.4 (Sept. 2022), p. 042003. ISSN: 0029-5515, 1741-4326. DOI: 10.1088/1741-4326/ac1654. (Visited on 10/21/2024).
- [79] United States Congress. *Energy Policy Act of 2005*. H.R. 6, 109th Cong. (Aug. 8, 2005), became Public Law 109-58. U.S. Government Printing Office, 2005. URL: <https://www.congress.gov/bill/109th-congress/house-bill/6>.
- [80] Paul M. Grant and Thomas P. Sheahan. *Cost Projections for High Temperature Superconductors*. Tech. rep. EPRI, Palo Alto, CA 94304; SAIC, Gaithersburg, MD 20878. Palo Alto, CA and Gaithersburg, MD: Electric Power Research Institute (EPRI) and Science Applications International Corporation (SAIC), 2002.
- [81] David Dalton. “Westinghouse Wins \$180 Million Contract For Assembly Of ITER Vacuum Vessel”. In: *NucNet* (July 2025). Accessed: 2026-02-10. URL: <https://www.nucnet.org/news/westinghouse-wins-usd180-million-contract-for-assembly-of-iter-vacuum-vessel-7-3-2025>.
- [82] Rémi Delaporte-Mathurin Samuele Meschini Sara E. Ferry and Dennis G. Whyte. “Modeling and analysis of the tritium fuel cycle for ARC- and STEP-class D-T fusion power plants”. In: *Nuclear Fusion* (2023).
- [83] L. M. Waganer. *ARIES Cost Account Documentation*. Tech. rep. University of California, San Diego, 2013.
- [84] J. Sheffield et al. “Cost Assessment of a Generic Magnetic Fusion Reactor”. In: *Fusion Technology* 9.2 (1986), pp. 199–249. DOI: 10.13182/FST9-2-199. URL: <https://doi.org/10.13182/FST9-2-199>.